NOVEL METHOD OF THE QUANTIFICATION OF TURBULENT FLUID FLOW IN SILICONE ARTERY PHANTOMS USING ACOUSTIC ANALYSIS

A Thesis

presented to

the Faculty of California Polytechnic State University,

San Luis Obispo

In Partial Fulfillment

of the Requirements for the Degree

Master of Biomedical Engineering in Blended MS BMED Program

by

Julia Wong

November 2023

COMMITTEE MEMBERSHIP

TITLE:	Novel Method of the Quantification of Turbulent Fluid Flow in Silicone Artery Phantoms Using Acoustic Analysis
AUTHOR:	Julia Wong
DATE SUBMITTED:	November 2023
COMMITTEE CHAIR:	Michael Whitt, Ph.D. MBA Professor of Biomedical Engineering
COMMITTEE MEMBER:	David Clague, Ph.D. Professor of Biomedical Engineering
COMMITTEE MEMBER:	Justin Shaw M.S. Aerospace Engineering

ABSTRACT

Novel Method of the Quantification of Turbulent Fluid Flow in Silicone Artery Phantoms Using Acoustic Analysis

Julia Wong

Cardiovascular disease is the leading cause of death globally and is responsible for taking 17.9 million lives per year. Despite the use of clinical treatments and detection methods, there remains a large population of individuals that suffer from CVD whose symptoms are left undetected and untreated prior to a life-threatening cardiac event. This highlights a need for an early detection method that can prevent the manifestation and worsening of the disease as well as address limitations of current early detection methods. An area of interest for early detection of CVD is subclinical atherosclerosis, which is the long, early, asymptomatic stage of plaque formation. Subclinical atherosclerosis has been namely associated with endothelial dysfunction and is the result of the pathological state of the endothelium due to its impact on vascular homeostasis, thrombosis, and vascular tone. Endothelial dysfunction is a result of several factors contributing to and promoting inflammation and results in changes in biological pathways that can alter the surface of the endothelium. This surface modification or added roughness changes the flow profile from laminar to turbulent flow due to the decreased shear stress on the vascular wall. Current detection methods such as carotid intima media thickness (CIMT) and flow-mediated dilation (FMD) targeted at identifying the early stages of atherosclerosis present limitations such as identifying late-stage effects of plaque formation and subjective readings highlight the need for a different approach to early detection. This experimental study aims to present a possible method of detecting the morphological changes of the endothelium due to inflammation through acoustic analysis of flow. Three silicone artery phantom groups were created with different degrees of inner diameter surface roughness to explore the relationship between relative roughness and sound associated with fluid flow. The results of this study are power spectral density graphs (PSD) which show frequency peaks associated with each of the phantoms at a theoretical laminar and turbulent Reynolds number. The PSD graphs show that there is a difference in frequency response between a smooth and rough artery phantom at the same flow rate providing preliminary support that sound analysis of fluid flow could provide information regarding early-stage cardiovascular disease.

Keywords: subclinical atherosclerosis, relative roughness, endothelial dysfunction, acoustic analysis

ACKNOWLEDGMENTS

I would like to thank my thesis advisor Dr. Michael Whitt for his unconditional support during this project and during my time at Cal Poly SLO. He has and continues to inspire me to be inquisitive, thoughtful, and approach life with kindness and positivity.

This is dedicated to my family for all their love and support throughout this experience.

TABLE OF CONTENTS

LIST OF TABLES

Table Page

LIST OF FIGURES

Chapter 1

INTRODUCTION

1.1 Statement of the Problem

Cardiovascular disease (CVD) is currently the leading cause of global mortality, taking an estimated 18 million lives per year. As of 2020, approximately one-third of all diseases around the world are attributed to the underlying effects of cardiovascular disease, or more specifically coronary artery disease (CAD). Coronary disease is the most common type of CVD and is caused by the thickening of arterial walls along with the narrowing or blockage of the coronary arteries due to an accumulation of plaque. This limits the amount of blood that travels to the heart, increasing the likelihood of cardiovascular complications such as a myocardial infarction, heart arrhythmias, or heart failure. Despite the fatal consequences of this disease, nearly 300,000 Americans each year die from CAD without having presented any symptoms [1].

Currently in the United States the two main methods of calculating risk of cardiovascular disease are the atherosclerotic cardiovascular disease risk calculator (ASCVD) generated by the American College of Cardiology (ACC) and the American Heart Association (AHA), shown in Figure 1, and the Framingham Risk Score.

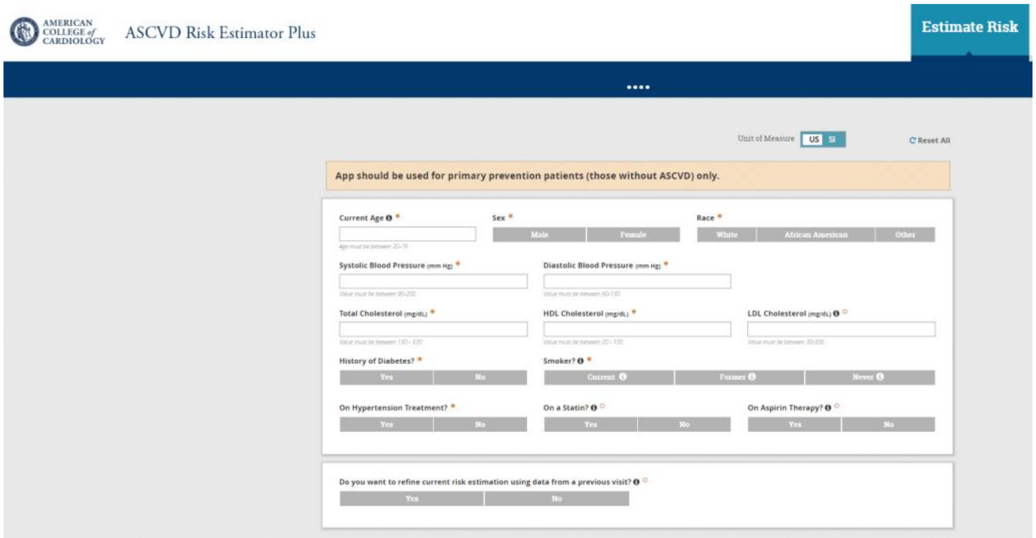

App should be used for primary prevention patients (those without ASCVD) only.

Do you want to refine current risk estimation using data from a previous visit?

Figure 1. American College of Cardiology ASCVD Risk Estimator Plus Survey [4].

In general, both methods provide a 10-year risk score for the manifestation of cardiovascular disease and relevant treatments to individuals based on their age, gender, cholesterol and blood pressure levels, diabetes and smoking status, and family history. However, current risk scores highlight the limitations in these methods through the wide variation in scores between populations as well as the high importance in sex and race specific equations when calculating scores [2]. This emphasizes the benefit of using continued risk screening using scores in parallel with disease screening to increase the effectiveness of CVD prevention by addressing limitations due to individual, economic, social, environmental, and psychosocial factors that affect individuals differently.

Disease screening for CAD acts as a method of early detection by identifying an individual at risk through the characterization of physiological parameters and subsequently implementing a treatment plan to prevent the manifestation or progression of the disease. More specifically, through identifying the preclinical or beginning stages of atherosclerosis, the primary cause of coronary artery disease, severe cardiovascular and overall health-related complications can be prevented. A primary marker of subclinical atherosclerosis is endothelial dysfunction or a disruption in the role that normal endothelium plays in the dynamic maintenance of vascular tone, homeostasis, angiogenesis, and hemostasis. The current gold standard of a non-invasive assessment of endothelial dysfunction is using flow-mediated dilation (FMD). FMD is a technique which measures the change of the brachial artery diameter and blood velocity in response to shear stress induced by arterial occlusion through inflation of an arm cuff. This method is paired with the generation of B-mode ultrasound images of changes in the diameter of the brachial artery. However, despite its wide use in clinical settings, this methodology has several limitations such as expensive equipment and operator training, lack of standardization, operator subjectivity, and high day-to-day variability which strongly impact readings [3]. This highlights the need for an objective method of quantifying endothelial dysfunction to detect subclinical atherosclerosis more accurately as a prevention method for plaque accumulation and coronary artery disease. The purpose of this report is to (1) replicate inflammation in arteries through the manufacturing of roughened silicone phantoms, (2) perform flow experiments that mimic disturbed flow, (3) identify a difference between low and high Reynolds flow using sound detection and analysis, and (4) relate findings to subclinical atherosclerosis.

CHAPTER 2

LITERATURE REVIEW

2.1 Subclinical Atherosclerosis

Subclinical atherosclerosis is an asymptomatic disease identified by the narrowing of artery walls due to a buildup of plaque composed of fat, cholesterol, calcium, and other substances found in blood [4]. It is characterized as a long phase within the timeline of plaque accumulation in which there are physiological and morphological changes to the arteries without the presence of identifiable symptoms. The difficulty in detection of this disease lies with the inability of clear, showing symptoms which ultimately prevents any form of treatment from mitigating further plaque accumulation or physical and cognitive injuries.

The pathophysiology of atherosclerosis can generally be defined in four main phases: lesion initiation, fatty streak, fibrous plaque formation, and calcification [5]. In general, subclinical atherosclerosis is caused by any physical injury or stress to the endothelial cells that line blood vessels such as diabetes, hypertension, high cholesterol, and smoking. Atherogenesis, the formation of plaque in arteries, is generally initiated in response to endothelial dysfunction, retention and modification of low-density lipoproteins (LDL), and other factors that promote the activation of endothelial cells. This inflammation leads to the recruitment of monocytes and vascular smooth muscle cells that work to capture and ingest modified LDLs which gives rise to foam cells, a macrophage that localizes fatty deposits in the arterial wall, shown in Figure 2. The accumulation of lipids in these foam cells lead to a fatty streak formation, a lesion on the luminal surface that is visible with the human eye and is the hallmark of atherosclerotic plaque formation.

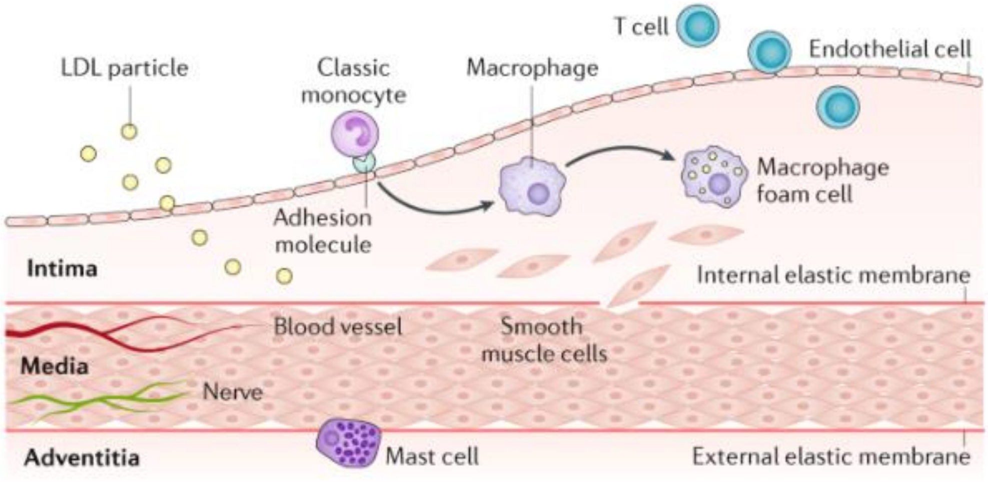

Figure 2. Formation of Foam Cells [6].

The transition from fatty streak to fibrous plaque formation and intimal growing within the artery is characterized by the presence of a necrotic core and fibrous cap, a defining feature in advanced atherosclerosis. The necrotic core is formed during the development of atherosclerosis in which apoptosis increases in response to increased monocyte and VSMC activity. This accumulation of apoptosis overwhelms macrophages and results in a release of inflammatory components, shown in Figure 3.

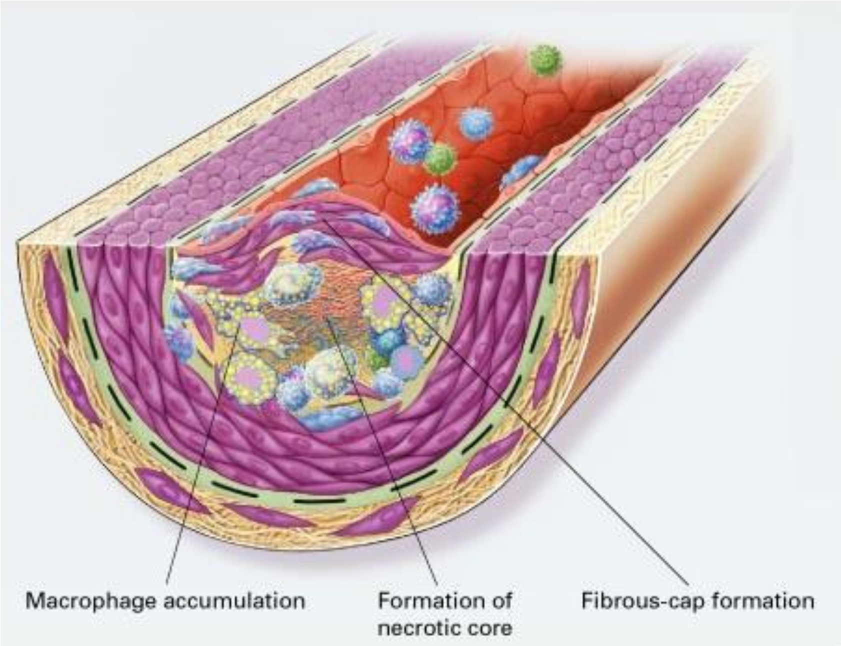

Figure 3. Cross-section of Artery with Formation of Necrotic Core and Fibrous Cap [7].

The formation of the fatty streak marks a stage in the progression of plaque formation in which the necrotic core, which constitutes the nucleus of the atherosclerotic plaques, increases in size due to the release of inflammatory components. This growth allows for an environment that promotes oxidative stress, thrombogenicity, and neighboring cell death. During this developmental process, fibers encapsulate the necrotic core and act as a support to stabilize and protect the core. The groups of fibers are called the fibrous cap and is a subendothelial barrier between the lumen of the artery and the core. The next stage towards the manifestation of atherosclerosis is the calcification of fibrous plaque. The process of vascular calcification of atherosclerotic lesions is currently a large area of study due to the difficulty of determining the source that triggers calcification because of the several confounding inflammatory factors [9]. However, a popular and well-studied theory points to macrophage and endoplasmic reticulum (ER) stress as the initiator of plaque calcification. A high-level overview of the process of calcification involves various overlapping phases of inflammation and inflammation resolution, as calcification is closely associated as a healing process to stabilize tissue or foreign bodies. In the context of plaque calcification, M2 macrophages play a large role in this healing process. More specifically, M2 macrophages are known to play a role in the regeneration of injured tissues after chronic or acute inflammation, similarly, M2 macrophages plays a role in calcification through promoting osteoblastic-like differentiation and maturation of vascular smooth muscle cells [9].

The pathophysiology of plaque formation and the manifestation of subclinical atherosclerosis is a complex and inflammatory-dependent pathway that has clearly defined phases. The presence of risk factors such as hypertension, high cholesterol, diabetes, smoking history, and family history of cardiovascular disease increases the likelihood of creating an inflammatory environment which allows for the formation of plaque. The difficulty with preventing the progression of subclinical atherosclerosis to its symptomatic counterpart is the lack of presentable symptoms in an individual despite the functional deterioration of the artery such as increased stiffness and the morphological deterioration presented as intima media thickness. Therefore, the method of detecting, characterizing, and categorizing the presence and severity of subclinical atherosclerosis is extremely important.

2.1.1 Detection Methods

The high incidence rate and the long asymptomatic phase of atherosclerosis makes early detection and disease screening methods highly valuable in the progression of the disease. Currently, the traditional method for screening for the presence of plaque, determining the risk of a cardiovascular event, and evaluating the degree of subclinical atherosclerosis is coronary angiography. A coronary angiography procedure, shown in Figure 4, is a minimally invasive procedure in which a catheter is inserted through the femoral artery access point and x-ray contrast dye is injected into the right coronary artery.

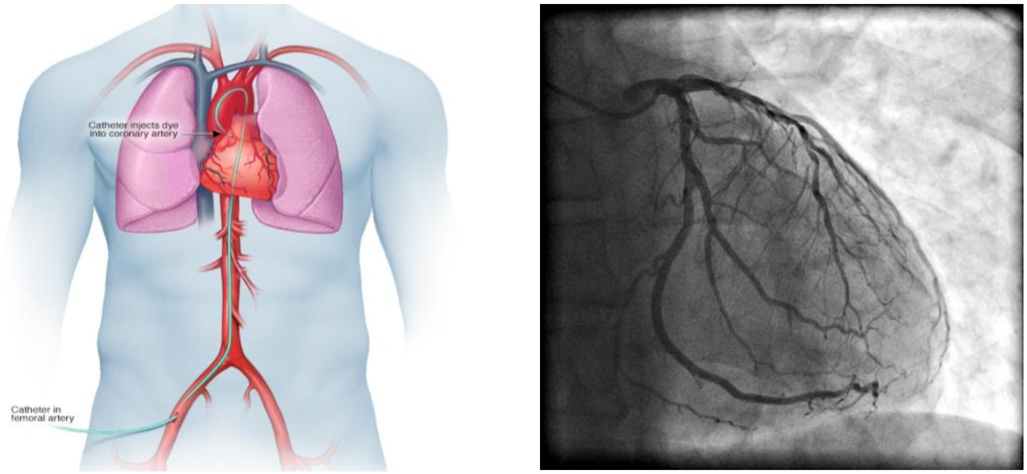

Figure 4. Coronary Angiography Access Point and X-ray Image of Arteries [10].

The purpose of this test is to show potential narrowing or blocking of the artery with high accuracy and sensitivity for detecting coronary stenoses [11]. Technological advancements such as computed tomography have been paired with this existing diagnostic method and have improved the ability to visualize atherosclerotic lesions in the vessel wall, characterize the degrees of calcification, and make the process non-invasive [13]. However, despite the improvements made to this process, there remains the issue of determining the role that coronary angiography and subsequent measurements play in early detection. More specifically, coronary angiography may improve patient outcomes by characterizing and confirming plaque formation or the blockage and narrowing of arteries through implementation of treatments earlier, but it does not address the disease at a stage in which regression is possible.

Another method for identifying the presence of subclinical atherosclerosis is carotid intima media thickness (CIMT). CIMT is a method of non-invasively measuring the thickness of the intimal and medial layer of the carotid artery wall using high resolution B-mode ultrasound imaging and has been closely associated with being a valuable surrogate marker for CAD, shown in Figure 5 [14], [15].

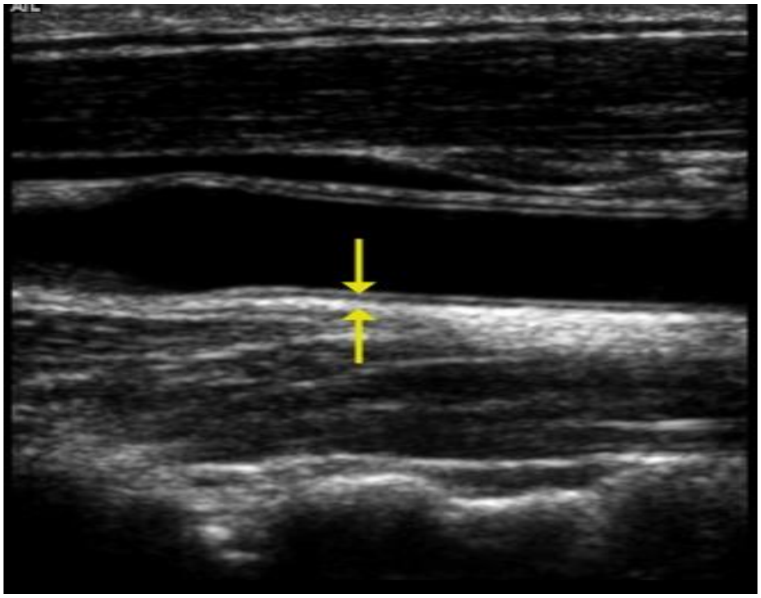

Figure 5. Carotid Intima Media Thickness Ultrasound [16].

The thickening of the intimal wall is largely due to the morphological changes that occur during atherogenesis due to high cholesterol level and lifestyle habits such as smoking and lack of exercise which allows it to act as mirror for atherosclerotic burden [17],[18]. This method is widely used in clinical applications due to its ease of use, precision, and reproducibility when determining measurements; however, there are concerning limitations to this process. The first concern is the subjectivity of reading CIMT measurements due to the lack standardization. Similarly, due to the lack of standardization of methods there have been shown to be large variation between relevant studies because of differences such as clinical study design, end points, population, sample size, duration between follow-ups, segment of carotid that is measured, semi-automatic versus manual ultrasound readings, and the image view of the measurement site. Therefore, without standardization, CIMT measurements must be analyzed and considered with other important variables to determine whether results should raise immediate health concerns regarding atherosclerosis and cardiovascular disease. For example, including variables such as sex, race, and evaluation of social determinants of health for an individual alongside quantitative CIMT measurements may be able to provide a more holistic overview of atherosclerotic burden.

However, similar to the diagnostic process of a coronary angiography to detect atherosclerotic burden and the severity of plaque formation, CIMT does not address the issue of early detection as it relies on the detection of significant morphological changes that lead to the increase in thickness of the intima and medial layers of the arterial wall. The limitations of both imaging techniques highlight the gap in screening for subclinical atherosclerosis as the measurement subject in both methods normally identify an advanced stage of disease progression in which aggressive treatments are necessary and regression is nearly impossible. The effects of this process are only exacerbated by the low likelihood of an individual with no symptoms undergoing a coronary angiography or CIMT. Therefore, there is a strong need for an early detection method for subclinical atherosclerosis that can objectively identify and characterize markers associated with the development of functional and morphological changes in the arterial wall prior to advanced plaque formation.

2.2 Endothelial Health

Endothelial dysfunction (ED) plays an important role in pathophysiology and manifestation of atherosclerosis and cardiovascular disease. In general, a healthy endothelium plays an essential role in maintaining cardiovascular health through regulating homeostasis, hemostasis, and vascular tone as well as modulating inflammation, and maintaining vascular growth [19]. However, when the endothelium is in a diseased state it is unable to maintain the regulatory functions of balancing anti-atherogenic and atherogenic properties which leads to an increase in thrombosis, inflammation, oxidant activity, and vasoconstriction [20]. A prolonged state of endothelial dysfunction plays a major role in the initial generation of plaque as well as in promoting continuous plaque growth which ultimately leads to a decrease in the reactivity and vascular tone of arteries. The impact of ED on promoting plaque formation in the different stages of atherosclerosis has made it an increasingly relevant research topic as an indicator for early detection of atherosclerosis. The severity of an activated endothelium on cardiovascular health highlights the importance of understanding the (1) pathophysiological progression to a diseased state, (2) biological response to a diseased state, and (3) existing methods to quantify endothelial health.

The vascular endothelium is composed of a monolayer of polarized endothelial cells (EC) which acts as a barrier between blood and tissue. The ECs that make up an endothelium are thin and elongated with a length, width, and thickness of approximately 30-50, 10-30, and 0.1-10 micrometers, respectively and are oriented along the axis of a vessel, shown in Figure 6.

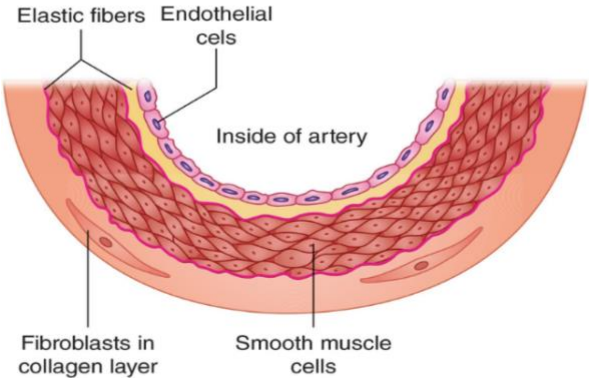

Figure 6. *Cross Section of Endothelial Layer [21].*

Due to the positioning and location of endothelial cells, the luminal membrane is exposed to circulating blood, while the basolateral surface is further distal to the blood flow and segregated from surrounding tissue by a glycoprotein basement membrane. The relationship between ECs and cardiovascular health is largely attributed to the ability of endothelial cells to sense and respond to changing mechanical and biological stressors to maintain an atheroprotective balance. Therefore, it is important to note how the endothelium responds to different hormones, vasoactive factors, and neurotransmitters, and mechanical stress to perform various vascular functions, such as maintaining vascular tone and homeostasis, promoting anti-inflammatory and anti-thrombotic environment through the regulated release of different hormones.

2.2.1 Function of a Normal Endothelium

One of the most important functions of a healthy endothelium is the maintenance of vascular tone and homeostasis which is defined by a balance of vasodilating and vasoconstricting molecules. More specifically, the maintenance of vascular homeostasis is determined by the controlled synthesis of two opposing molecules, nitric oxide (NO) and angiotensin II (A_{II}).

Nitric oxide is a biologically active volatile gas that is present in almost all tissues and is a key player as a stimulus that promotes vasodilation as well as numerous other vasoprotective and anti-atherosclerotic functions. The production of NO in endothelial cells relies on the enzyme endothelial nitric oxide synthase (eNOS) which functions within the L-arginine-NO pathway to transform L-arginine into NO and L-citruline, shown in Figure 7.

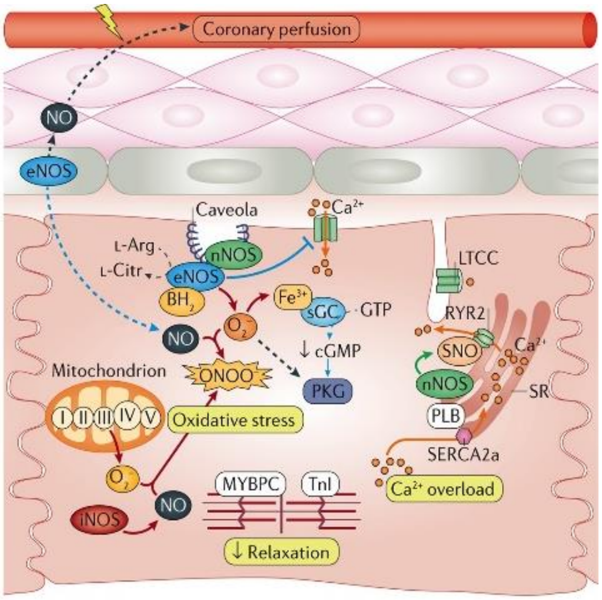

Figure 7. L-arginine-NO pathway [22].

More specifically, the production of NO is activated by increasing levels of intracellular calcium ions, which induces the binding of the molecule of calmodulin (CaM) to eNOS, which leads to eNOS activation. An activated eNOS enzyme further works to catalyze L-arginine to generate NO and L-citruline due to the phosphorylation by protein kinase B (PKB) on Ser 1177 and dephosphorylation by protein phosphatase PP1 and PP2A on Thr495 [23]. The NO produced from this pathway then diffuses across the cell membrane of an endothelial cell into a vascular smooth muscle cell (VSMC) where GTP is degraded, and cGMP is released and regulates cytosolic Ca $^{2+}$ and is responsible for smooth muscle fiber relaxation. NO production is stimulated by the binding of agonists like bradykinin and acetycholine which increase the presence of intracellular Ca^{2+}, however another source of stimulation that is extremely important for NO release is mechanical stressors such as hemodynamic shear stress and intraluminal pressure [24]. These mechanical stresses can stimulate eNOS activation and subsequent NO release in three main endothelial-dependent avenues. One way of stimulation is the opening of mechanosensing ion channels (MSICs) which occurs as a response to an external stress on the endothelial cell and mediates the influx of calcium ions into the cell. Another way mechanical stresses stimulate NO production is the deformation activation of G-protein coupled receptors (GPCRs) which allow the release of intracellular calcium ions. The last method of stimulation is through the application of hemodynamic shear stress which stimulates integrins to activate phosphatidylinositide 3-kinases (PI3K) enzymes and allow for intracellular calcium release.

While NO production and diffusion to vascular smooth muscle cells promote vasodilation and vasorelaxation, Angiotensin II (A_{II}) works to induce vasoconstriction to promote a balanced, healthy vascular tone. In general, A_{II} is a multifaceted hormone that uses several signaling pathways to target various organs such as the kidney which results in sodium and water retention and arteriolar vasoconstriction, the adrenal gland which stimulates aldosterone secretion, the brain which activates the sympathetic nervous system, and the vascular system which causes vasoconstriction. Angiotensin II is the product of the renin-angiotensin system (RAS) and is responsible for inducing the inflammatory responses seen in its effector target organs. RAS begins in the kidney where the enzyme renin is released by juxtaglomerular cells in response to decreased sodium delivery and sympathetic activation while in the liver, the protein Angiotensinogen is produced and is subsequently cleaved by renin to produce the hormone Angiotensin I. This inactive hormone circulates in the bloodstream until it encounters and is cleaved by angiotensin-converting enzyme (ACE) which is produced in the lungs. Angiotensin I is reduced into several pieces, one of which is the active hormone, Angiotensin II that continues to travel in the circulating blood and target different organs [25]. In the systemic arterioles, A_{II} binds to G protein-coupled receptors which causes in vasoconstriction through a series of second messenger cascades and counters the vasodilation and vasorelaxation effects of the presence of nitric oxide in vascular smooth muscle cells. However, despite the presence of $A_{II,}$ a hallmark of a healthy endothelium favors high levels of nitric oxide displayed by a vasodilatory phenotype [26].

Another important function of the endothelium is promoting an anti-inflammatory, antithrombotic, and atheroprotective environment. The ability of endothelial cells to foster such an environment relies on the numerous, well-regulated pathways that allow for the downregulation of proteins and hormones that induce an inflammatory response. Of the many factors that promote endothelial health and endothelial cell survival, the mechanosensing and response of laminar shear stress (SS) is one of the most influential. Laminar and high shear stress, displayed commonly in straight portions of vasculature, promotes endothelium health in several ways including inhibiting tumor necrosis factor-α (TNF- α) pathways and upregulating thrombomodulin (TM) [27].

TNF-α is a major inflammatory cytokine that is involved in several pathways and responses which are related to disease pathogenesis and manifestation. This cytokine is primarily known to participate in leukocyte adhesion, the production of reactive oxygen species (ROS), and the activation of other transcriptional factors that increase vascular inflammation. TNF-α affects the endothelium through impairing endothelium-dependent and nitric oxide mediated vasodilation which results in a decreased production and increased removal of NO. The effects on eNOS and NO production have detrimental effects on the regulation of vascular tone and homeostasis as this environment favors vasoconstriction which can lead to hypertension and manifest into more severe conditions. However, in a healthy endothelium, the effects of TNF-α are inhibited by the presence of high shear stress conditions which prevent related G-protein coupled and calcium mobilizing pathways which mediate endothelial cell apoptosis and inhibit other secondary, intracellular signaling pathways which promote inflammation [28].

2.2.2 Endothelial Dysfunction

The functions of the endothelium are widespread and work in unison to promote the overall health of the vasculature by maintaining vascular tone and homeostasis, promoting an anti-inflammatory environment, and regulating the activation and inactivation of signaling pathways that contribute to vascular health. However, in an activated or diseased state, the endothelium is unable to perform these essential functions which leads to the pathogenesis of inflammatory diseases such as atherosclerosis. Endothelial dysfunction is defined as an activated state of the endothelium in which there is an increase in reactive oxygen species (ROS), an increase in proinflammatory factors, a deficit of nitric oxide (NO) bioavailability, and altered vascular reactivity.

This atherogenic phenotype or activated endothelium is induced by consistent, long-term exposure to traditional cardiovascular risk factors such as smoking, lack of exercise, obesity, and hypertension which promote a systemic inflammatory response that invokes an innate immune response. In general terms, a healthy endothelium produces NO via eNOS and newly produced nitric oxide target key regulatory molecules and inhibits the activation of specific cellular processes. The state of a healthy and functional endothelium is marked by a phenotype in which the production of NO silences these cellular pathways. However, in the presence of risk factors, the innate immune response is activated and alters the function of eNOS from NO production to ROS production like H_2O_2, which is referred to as an uncoupled eNOS. Endothelial dysfunction is not marked by the production of ROS by eNOS, but instead by the long-term exposure to harmful risk factors and subsequent sustained production of these inflammatory reactive oxidative species which affect the endothelium. This environment results in altered endothelial cell function and affects the maintained homeostasis that promotes an anti-inflammatory system [29].

The manifestation of endothelial dysfunction is multifaceted and can be attributed to several deviations from normal physiology that result in an increase in ROS, a decrease in bioavailable NO, and changes vascular dilation other than the presence of long-term risk factors and an uncoupled eNOS pathway. An important area of interest regarding the manifestation and physiological consequences of endothelial dysfunction is the role of shear stress in NO regulation, endothelial cell topography, and hemodynamics.

Shear stress is a factor of blood viscosity, velocity gradient, and flow type. Shear stress and endothelial cells have a close relationship as ECs respond to the mechanical changes and external stimuli caused by blood flow. An example of this is endothelium-dependent NO production and release stimulated by shear stress. In normal physiological conditions, endothelial cells respond to shear stress by elongating and aligning to the direction of flow however when exposed to low and oscillating levels of shear stress, endothelial cells proliferate and express adhesion molecules and chemotactic factors which result in an inflammatory response. Chronic inflammation caused by prolonged exposure to cardiovascular risk factors result in changes in endothelial cell morphology, hemodynamics, and shear stress. An inflamed state induces a morphological change in the surface topology of the endothelium and is thought to increase the overall surface roughness and cause cell misalignment [30]. The effects of an increased surface roughness have been studied to be responsible for the change of blood flow from steady, laminar to disturbed, oscillatory, and turbulent in these specific regions. The effects of inflammation and changes in normal endothelial cell health and morphology are only further exacerbated by the presence of turbulent flow as it continues to cause damage to the monolayer and promotes endothelial cell turnover [31].

Another component to a state of inflammation is the change in the degree of shear stress, which is also determined by ECs, flow type and velocity. In laminar flow, the physiological levels of shear stress and the frictional forces against the walls are at a level that promote pro-atherogenic factors and maintain the health of the endothelium through signaling pathways such as eNOS. In contrast, disturbed flow decreases the about of frictional force against the vessel wall and the produced shear stress cannot activate signaling pathways to produce the necessary amount of nitric oxide, ultimately causing a shift in balance towards vasoconstriction.

Endothelial dysfunction plays an important role in the progression and manifestation of atherosclerosis. The activated state of the endothelium not only promotes an inflammatory response that invokes change in the morphology of endothelial cells, but also majorly contributes to plaque progression and growth. Prolonged exposure to risk factors coupled with chronic inflammation allows endothelial cells to reach an activated state in which morphological changes occur, flow is disturbed, NO bioavailability is decreased, and the pathogenesis of atherosclerosis begins.

2.2.3 Detection Methods of Endothelial Dysfunction

Endothelial dysfunction plays an impactful role in the progression to and manifestation of plaque formation, also known as atherosclerosis. The presence of ED signifies the earliest marker of inflammation, prior to any noticeable changes to anatomy or recognizable symptoms, which make it a desirable measurand for the early detection of subclinical atherosclerosis. Currently, there are several invasive and non-invasive methods to determine endothelial health including measuring coronary artery diameter changes and flow-mediated dilation. The gold standard for evaluating coronary endothelial function is through intra-arterial administration of acetylcholine which promotes vasodilation. The changes in vessel diameter are subsequently measured by quantitative coronary angiography and changes in blood flow [32].

The result of an individual with endothelial function is a lack of dilation due to an increase in vasoconstriction induced by vascular smooth muscle cells and decreased NO bioavailability. An alternative method for evaluating endothelial dysfunction as an indicator of atherosclerosis is flow-mediated dilation (FMD) which measures vasodilation using a high-resolution B-mode ultrasound. FMD measures the endothelial-dependent dilation of the target vessel in response to reactive hyperemia by cuff inflation and deflation and subsequent increase in blood flow, shown in Figure 8.

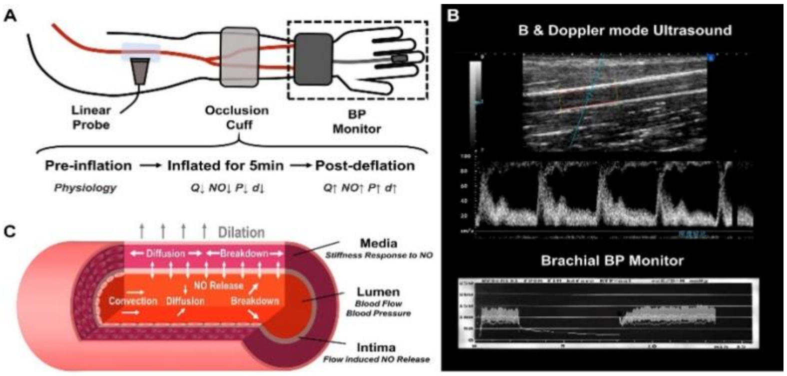

Figure 8. Flow-Mediated Dilation and Ultrasound [33].

More specifically, brachial artery FMD has been used as a hallmark measurement for endothelial function by inducing an increase in flow, shear stress, and activation of NO pathway. FMD is widely used, however there are concerning limitations that prevent this non-invasive method from being used as a standardized procedure for early detection or risk for atherosclerosis. FMD limitations include heavy reliance on subjective image analysis and variable baseline data because it is currently not a standardized process. Similarly, FMD shows high variation and poor reproducibility between operators.

2.3 Fluid Dynamics

Flow type plays an important role in the promotion of endothelial dysfunction and progression of plaque formation due to the relationship between turbulent flow or disturbed flow and shear stress. More specifically, oscillatory and disturbed flow is associated with subsequent low shear stress which results in pathogenic responses from the endothelium such as decreased NO production and upregulation of inflammatory cytokines. The important role that hemodynamics plays in the manifestation and regulation of vascular health has made understanding the mechanics of fluid flow a relevant and widely researched topic for experimentation and modeling.

In general, fluid flow analysis can be used to model and understand the complexities of the cardiovascular system through experimental and theoretical observations. In this study, the main area of research is internal flow within an elastic tube. Generally, flow behavior can be categorized as either laminar or turbulent depending on the ratio of inertial to viscous forces in the fluid, which is defined by the Reynolds number which determines the relationship between inertial and viscous forces, shown in the Equation 1.

$$Re = \frac{\text{Inertial Forces}}{\text{Viscous Forces}} = \frac{\rho\ V\ D}{\mu} \tag{1}$$

ρ = fluid density V = velocity

D = diameter of vessel μ = dynamic viscosity

The variables included in Reynolds equation represent the fluid density, average velocity, length of the vessel, and dynamic viscosity of the fluid. The Reynolds number determines the type of fluid flow that exists within a vessel based on the variables shown above and abides by the general rule for a smooth pipe that flow is laminar when Re ≤ 2300, flow is turbulent when Re > 3500, and flow is transitional when Re ≈ 23000

Error! Reference source not found.[34]. However, these cut-off values for flow type vary depending on the source. When the Re number is small or moderate, inertial forces can be suppressed by viscous forces and the result is an aligned streamline or laminar flow whereas when the Re number is large, inertial forces are dominant and viscous forces are unable to prevent streamline fluctuations of the fluid seen in turbulent flow.

2.3.1 Laminar vs. Turbulent Flow

Laminar flow is described as a flow type in which fluid particles move in smooth layers, or laminas whereas in turbulent flow, high-frequency fluctuations exist and result in random motion throughout the fluid. The transition from laminar to turbulent flow is heavily dependent on various factors such as geometry type, temperature, flow velocity, fluid type, and surface roughness. However, the variable of interest in this study is surface roughness and its effect on pressure drops and friction along the length of a vessel. In fully developed laminar flow through a vessel with a constant diameter, the pressure drops uniformly along the pipe length which can be represented using the Hagen-Poiseuille equation, shown in Equation 2.

$$\Delta\mathrm{P} = \frac{8\mu L Q}{\pi R^4}$$

(2)

μ = dynamic viscosity	L = length of vessel
Q = volumetric flow rate	R = radius of vessel

Hagen-Poiseuille can be written to solve for the pressure drop, $\Delta\mathrm{P}$, when μ, the dynamic viscosity, L the length of the vessel, Q the volumetric flow rate, and R the radius of the vessel are known. Hagen-Poiseuille is derived from the three-dimensional Navier-Stokes equations assuming that steady state flow, radial and swirl components of velocity are equal to zero, flow is asymmetric, and flow is fully developed. The Navier-Stokes equations describe the motion of incompressible fluids relating the velocity, pressure, temperature, density, and viscosity and can be described as the conservation of momentum.

However, it is important to discuss the viscous effects on energy considerations, namely the conversion of mechanical to thermal energy caused by friction. This can be described by Bernoulli's Equation of energy balance which can determine the pressure difference between any two points when zero frictional effects are accounted for shown in the equation 9.

$$\left(\frac{p_1}{\rho g} + \frac{\overline{V_1}}{2g} + z_1\right) = \left(\frac{p_2}{\rho g} + \frac{\overline{V_2}}{2g} + z_2\right)$$

(3)

More specifically, the average velocity between two given points can be described in terms of pressure and position when using Equation 3, which is derived from integrating the steady, inviscid form of the Navier-Stokes equation. However, realistically there will be energy losses and transformation in any system so Bernoulli's Equation may be adjusted to account for frictional losses that may occur during fluid flow and can be represented by the equation:

$$\left(\frac{p_1}{\rho g}+\alpha\frac{\overline{V_1}}{2g}+z_1\right)-\left(\frac{p_2}{\rho g}+\alpha\frac{\overline{V_2}}{2g}+z_2\right)= H_{lT}$$

(4)

In which p is pressure at point 1 and 2, ρ is fluid density, g is gravity, α is the kinetic energy coefficient, $\overline{V}$ is the average velocity, and z is the y-direction position at point 1 and 2.

Equation 4 represents the irreversible loss of mechanical energy due to frictional losses that occur through a vessel despite a constant area and diameter. For a horizontal pipe that can be described using Bernoulli's Equation of no losses, it assumes that α, the kinetic energy coefficient is 1 and H_{lT}, total head loss is 0. The kinetic energy coefficient, α, is used as a correction factor to account for the use of $\overline{\mathrm{V}}$, average velocity. However, when frictional losses and energy conservation is applied as shown in Equation 2, the kinetic energy coefficient is assumed to be α = 2 for laminar flow and α = 1 for turbulent flow.

2.3.2 Frictional Losses, Relative Roughness, and the Moody Diagram

H_{LT} represents total head loss within a system and represents the sum of major losses h_l, due to frictional effects and minor losses, h_{lm}, due to the results of fittings and entrances. For fully developed flow assuming a constant-area vessel, horizontal pipe, and head loss minor is equal to 0, Bernoulli's Equation can be reduced to solve for major head loss as a function of pressure drop, shown in Equation 5 [34].

$$\frac{p_1 - p_2}{\rho} = \frac{\Delta p}{\rho} = h_l \tag{5}$$

Theoretically, due to the ability to solve for pressure drop in laminar flow analytically in Equation 5, major head loss can be also solved as a function of Reynolds number, length of vessel, diameter, and average velocity, shown in the equation 6.

$$h_l = \frac{64}{Re}\left(\frac{L}{D}\frac{\bar{V}^2}{2}\right) \tag{6}$$

However, due to the complexities of turbulent flow, the pressure drop along the length of the vessel excluding the entrance length cannot be determined analytically and experimental data is necessary. Instead, the pressure difference is a function of diameter and length of the vessel, pipe roughness, average velocity, fluid density, and fluid viscosity. This relationship can further be represented as major head loss in fully developed turbulent flow in Equation 7 as major head loss as a function of friction factor, vessel length and diameter and average velocity.

$$h_l = f\left(\frac{L}{D}\frac{\bar{V}^2}{2}\right)$$

(7)

The parameter f is Darcy friction factor and can be calculated with Equation 8, which uses known values of surface roughness on the vessel or pipe and diameter of internal flow.

$$f = \left(\frac{e}{D}\right)$$

e = pipe roughness D = diameter of internal flow

(8)

In fully developed flow, friction factor is determined experimentally using the Moody Diagram in Figure 9.

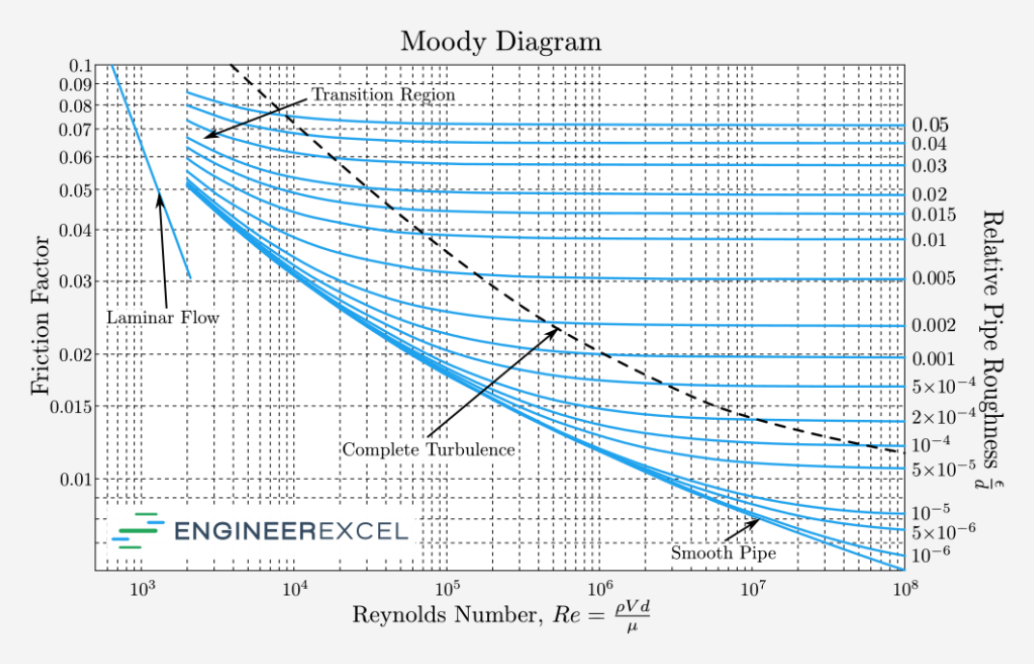

Figure 9. Moody Diagram [36].

This diagram is commonly used in unison with a calculated Reynolds Number and known relative roughness to determine the friction factor of the inner diameter surface through outlining the effects of increasing roughness on the Darcy-Weisbach friction factor and subsequent pressure drops. As highlighted in Figure 10, the Moody Diagram highlights the difference in how friction factor is calculated between laminar, transitional, and turbulent flow. In laminar flow, the friction factor is independent of surface roughness and is dictated by the Reynolds number such that increasing velocity within a constant-area pipe or vessel can transform into transitional or turbulent flow once the critical Reynolds Number is surpassed. In laminar flow, the velocity profile is parabolic with the maximum velocity existing at the center, however when the transitional Reynolds Number is surpassed and flow becomes turbulent, the velocity gradient flattens out subsequently resulting in highly oscillatory wall shear stress and an increased friction factor, shown in Figure 10.

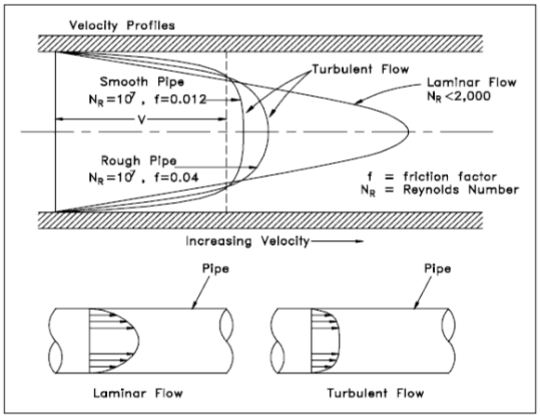

Figure 10. Velocity Profiles of Laminar and Turbulent Flow [35].

As the Reynolds number grows and flow becomes increasingly more turbulent, the thin viscous boundary layer decreases and the surface roughness begins to protrude the viscous sublayer and friction factor becomes a function of both the Reynolds number and relative roughness. In this case, the degree of roughness directly correlates to the drag or pressure loss that occurs along the length of the vessel or tube. In general, in laminar flow head loss is proportional to average velocity, in transitional flow there is a steep increase in head loss, and in the turbulent flow head loss continues.

Besides the use of the Moody Diagram, there are other methods of calculating or determining friction factor that are non-graphical such as the Colebrook equation, shown in Equation 9.

$$\frac{1}{\sqrt{f}} = -2.0\log\left(\frac{e/D}{3.7} + \frac{2.51}{Re\sqrt{f}}\right) \tag{9}$$

The Haaland equation shown in Equation 10 which exists as an approximation of the Colebrook equation and is used most accurately for Re > 3000.

$$\frac{1}{\sqrt{f}} = -1.8\log\left[\left(\frac{e/D}{3.7}\right)^{1.11} + \frac{6.9}{Re}\right]$$

(10)

Lastly, the Blasius correlation shown in Equation 11, used for turbulent flow in smooth pipes with Re ≤ 10^5.

$$f = \frac{0.316}{Re^{0.25}}$$

(11)

Aside from the frictional impacts on energy transformation in internal flow, minor head losses are present due to flow separation caused by various inlets and exits, changes in pipe sizes, or bends. All of which can be calculated using representative data to solve for minor head loss, shown in equations 12 and 13 [35].

$$h_l = f\left(\frac{L_E}{D}\frac{\bar{V}^2}{2}\right)$$

L = equivalent pipe length

(12)

$$h_l = K\left(\frac{\bar{V}^2}{2}\right)$$

K = experimental loss coefficients

(13)

2.4 Sound and its Fundamentals

Sound is defined as a form of energy created by vibrations that travel through mediums such as air or water in the form of longitudinal pressure waves, such that the propagation of waves is traveling in the same direction as its displacement. The main characteristics of sound may be described objectively in two ways. Firstly, by using its amplitude, measured by the distance from the baseline of the waveform to its crest or trough and secondly by using its frequency or the number of waves or compressions that are produced during a specified period of time. A common method of representing a sound wave is in reference to its intensity, power, or amplitude which can be measured using units of decibel (dB). Decibel is a logarithmic unit used to describe sound intensity and is derived from one-tenth of the unit Bel. It is represented as a relative measurement and can be expressed using the equation:

$$\mathrm{V_{dB}} = 10\log_{10}\left(\frac{\mathrm{P_2}}{\mathrm{P_1}}\right)$$

$\mathrm{V_{dB}}$ = difference in decibels P = power

(14)

Decibels can be expressed to represent the strength of a signal with reference to a variety of different units such as sound pressure, potency, and voltage which can all be expressed as dBSPL, dBw, and dBV, respectively. While sound frequency is represented in units of Hz and is shown in base units as (s^{-1}). However, perception of sound pressure waves plays an important role in understanding how these characteristics translate to discernible senses. For example, humans can hear due to the processing of sound waves that travel through the ear canal to the eardrum. The sound waves create vibrations that propagate to bones within the middle ear known as the malleus, incus, and stapes, highlighted in Figure 11.

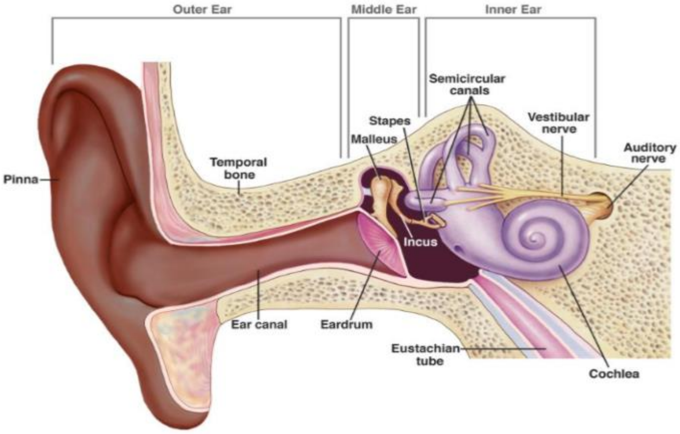

Figure 11. Sound Processing in the Human Ear [37].

The three middle ear bones amplify sound vibrations and send them to the cochlea, a fluid-filled structure that propagates sound waves through the fluid to the basilar membrane where hair cell movement creates an electrical signal that is propagated through the auditory nerve to the brain where the sound vibration is understood as a known noise [37]. Due to the variability in hearing ability and perception, the amplitude and frequency of a sound waveform translates to noise loudness and pitch, which can be experienced differently for every listener. More specifically, human hearing can detect frequencies in the range of 20 Hz to 20 kHz, whereas animals such as elephants can detect infrasound frequencies, or frequencies below 20 Hz. Frequencies over 20 kHz are known as ultrasound and are utilized are rarely detected and heavily used in diagnostic clinical settings.

2.4.1 Fourier Transform

Sound waves and acoustic analysis plays an integral role in a variety of different applications such as seismology, engine testing, and ultrasound imaging because of its ability to determine frequency components that make up a noise along with the power level associated with it. Sound and acoustics are commonly analyzed in the frequency domain because of the ability to identify behaviors and patterns more clearly and accurately within a signal that are undiscernible in the same waveform represented in the time domain. The method of translating between the two domains is a mathematical technique named the Fourier transform which transforms a continuous function or signal in the time domain into a function or signal in the frequency domain using the equation:

$$X(k) = \int_{-\infty}^{+\infty} x(t)e^{-j\omega t}dt \tag{15}$$

This function is reliant on the idea that a continuous function can be expressed or represented as a series or sum of sinusoids and as such a signal can be decomposed into constituent components and the frequencies that are present. This mathematical function can also be represented for signals that are not continuous and have a finite sequence of data and provides an equivalent approximation of a Fourier Transform and is known as the Discrete Fourier Transform (DFT), shown in the equation:

$$X(k) = \sum_{n=0}^{N-1} x(n)e^{-j\omega n}$$

(16)

A method of efficiently calculating the DFT of a function appeared with the algorithm the Fast Fourier Transform (FFT), in which the DFT is broken down into smaller DFTs to decrease the computation power and time required. The use of the FFT allows for quick conversion from the time domain to the frequency domain of a discrete signal. However, there are two main issues associated with using an FFT for signal transformation and analysis. The first is the issue of aliasing in which false lower frequencies appear in a transformed signal due to poor and inadequate sampling or representation of the original analog signal. The method of addressing this problem is to ensure that the sampling frequency, or the number of samples of the signal taken in 1 second, abides to the fundamental rule that the sampling frequency must be twice the number of the maximum frequency that a system can measure also known as the Nyquist frequency. The Nyquist theorem holds that the highest frequency can be given such that the sampling rate can accurately reconstruct the analog signal in the frequency domain, shown in the equation:

$$f_{Nyquist} = \frac{1}{2}\nu$$

ν = sampling rate

(17)

The second area of concern in using an FFT is leakage, which is the smearing of energy from such that a frequency is represented inaccurately as adjacent frequencies because the original signal being measured is not periodic. This results in the addition of unwanted frequencies, commonly at a lower amplitude. However, the issue of leakage can be remediated by the inclusion of windowing prior to performing an FFT. Windowing data is done by multiplying a data sequence with a user-defined window function of a certain width to create a weighted section for a portion of time. Several windows exist such as the Hanning, Kaiser-Bessel, and Bartlett windows which will provide different distortion characteristics using and reduces discontinuities along different areas of a waveform.

2.4.2 Representations of Spectral Acoustic Data

FFT analysis allows for efficient transformation of time dependent data into the frequency domain to provide information of excited frequencies, corresponding amplitudes, and harmonic content. However, acoustic data, specifically vibrations, can be represented in the form of power spectral density (PSD) graphs by using an FFT to transform data and detect harmonics and resonances that are unable to be identified in the time domain waveform. A PSD can be generated from an FFT by squaring the magnitude for each user-defined frequency bin to find an average which represents the power or mean-square value of the sound signal strength and is normalized to 1 Hz which results in a graph with units of power ($\frac{G^2}{Hz}$) and frequency (Hz), shown in Figure 12.

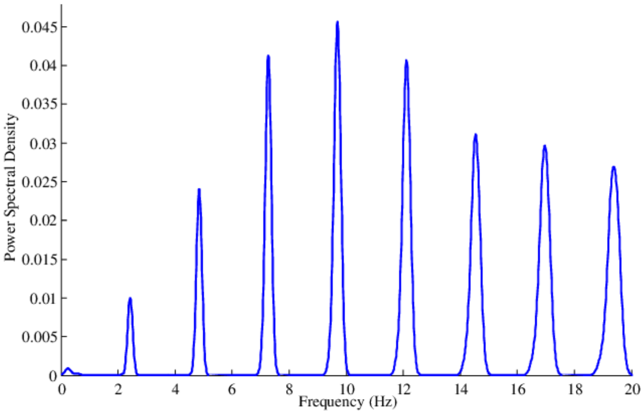

Figure 12. Example of a PSD graph of an ECG of a pediatric patient [37].

PSD graphs are commonly used to characterize noise, independently of the length of sample and can be used to analyze acoustic flow data. More specifically, it allows acoustics and vibrations to be represented as distributions of energy as a function of frequency and highlight the differences between strong and weak frequencies in the fluid sound which is especially useful for differentiating between different flow types in this application.

2.4.3 Acoustic Analysis of Flow

Acoustic and sound frequency analysis is a widely used technique for understanding fluid flow types and behaviors due to its ability to analyze vibrations caused by the generation of sound waves. Acoustic analysis plays a large role in the study of fluid mechanics for industrial uses like in the oil, aerospace, and biomedical sectors. More specifically in the biomedical space, research using acoustic measurements of fluid flow allows for a further understanding of the manifestation of disease through mechanistic elements related to fluid flow such as pressure differences, frictional influences, wave propagation, and flow type.

In biomedical applications, the use of acoustic analysis of flow is heavily used in research regarding the modeling and studies of turbulent flow subsequent vessel vibration and its relation to the manifestation of disease. Its use continues to be relevant due to the relationship between non-laminar flow and the disease states such as intima media thickening, plaque formation, and arterial stenosis [38]. Several studies have set the precedent for research relating to phonoangiography, the quantitative analysis of sound produced by blood flow. Relevant pieces of literature include the (1) comparison of spectra of fully developed turbulent pipe flow to stenotic murmurs, (2) investigation of sound spectra of turbulence and tube or wall vibrations, (3) determination of frequency spectrum induced by an arterial occlusion [[39], [40], [41]].

In 1970, Lees and Dewey performed an analysis on the sound spectra obtained from patients with known severe atherosclerosis using a piezoelectric displacement transducer and produced a time-resolved frequency spectrum. This data was compared to wall pressure fluctuations of turbulent flow through a pipe and found that the spectra of the two were similar and that the area distal to arterial occlusions or stenotic site exhibited fully turbulent flow which was insensitive to its Reynolds number [39]. Similarly, in 1977, Kim and Corcoran performed experimental studies to analyze a steady-state flow through a rigid tube with internal diameter of sharp-edges obstructions using a hot-film anemometer to measure velocity and turbulent fluctuations and subsequent measurement of the turbulence spectra. The results of the experimental study showed that sound spectra are dependent on the properties and geometry of the wall of the pipe or vessel used as peak frequencies differed between arteries with different wall thickness with the same inner diameter size and under identical test conditions. Kim and Corcoran found that the random turbulent flow through the pipe results in vibrations of the wall that are different from the turbulent spectrum.

In 1994, Akay and Welkowitz determined that turbulent flow associated with coronary stenosis in a canine produces a specific acoustic signature that is differentiable to a healthy artery with laminar flow due to the varying degree of vibrations caused by the disturbed blood flow. A Teflon bead with the same outer diameter of the artery was surgically placed into the arterial space and sound was recorded using a piezoelectric microphone on the skin surface, shown in Figure 13.

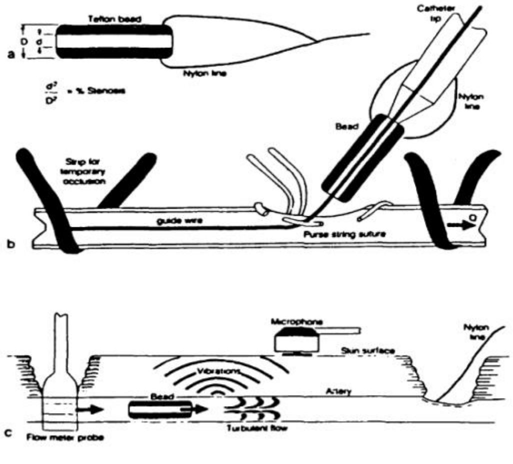

Figure 13. Experimental Set-Up of Akay and Welkowitz's Study [41].

Akay and Welkowitz tested different degrees of aortic stenosis by changing the diameter of the vessel and maintaining the Teflon bead size and found that there was a notable frequency difference between different degrees of arterial occlusion. This research provides a foundation for using auditory methods to analyze blood flow through diseased arteries and could be relevant regarding early detection of plaque formation and associated flow changes. More specifically, using sound analysis could play a role in determining and differentiating between laminar and turbulent blood flow associated with endothelial health, arterial inflammation, and the early stages of atherosclerosis.

CHAPTER 3

METHODOLOGY

3.1 Objective

The purpose of this study is to differentiate between laminar and turbulent flow sound frequencies associated with endothelial dysfunction through performing acoustic analyses of flow through silicone phantom arteries with varying degrees of relative roughness. This novel research study introduces a possible early detection or screening method for inflammation and endothelial dysfunction correlated with the pathogenesis and progression of atherosclerosis and other severe cardiovascular diseases. This proposed test method relies on the relationship between relative roughness, turbulent flow, and cardiac auscultation, such that flow type changes with respect to relative roughness and can be detected with acoustic analysis. The goal of this study is to identify a difference between a smooth and roughened silicone phantom artery and correlate any findings to a clinical application of using this type of cardiac auscultation as a screening method for at risk populations and asymptomatic patients.

3.2 Experimental Set-up

The experimental set-up of this study is composed of (4) main components, (1) silicone phantom arteries, (2) a BIOPAC contact microphone and Acq*Knowledge®* data-acquisition system, (3) flowmeter and water pump, and (4) two Deltran pressure transducers, all of which make up the test flow-loop system.

3.2.1 Silicone Phantom Arteries

The phantom arteries manufactured for this experimental study were molded using DragonSkin10 NV and have a length of 9.2”, outer diameter of 0.425”, inner diameter of 0.25”, and wall thickness of 0.0875”. The goal of the silicone phantom artery fabrication process was to create clinically relevant vessels that allow for consistent testing and data collection. However, in comparison to the average brachial artery diameter of 3.96 mm**,** the silicone phantom arteries are approximately four times the size of a native vessel due to the manufacturing method and limitations. The main limitations are due to the viscosity of the silicone used and the length requirement of each artery which cause incomplete curing, large air bubbles, and gaps in the mold. Therefore, for this benchtop model, a larger arterial diameter and wall thickness was used to perform acoustic studies. A total of 9 silicone arteries were manufactured and within this total were 3 different groups made up of 3 arteries each. Every experimental group had a specific surface roughness on the inner diameter of the artery to test the difference between the acoustics of laminar and turbulent flow.

The artery manufacturing process included 3 elements, a 3D-printed jig, 3 different mandrels, and DragonSkin10 NV silicone mold. The 3D-printed jig was designed to create a more consistent and time efficient method of molding arteries, as previous methods included plastic tubing which required an intricate vessel removal process. The jig is made up of 7 interacting pieces due to the desired length of the arteries and the volume limitation of the print bed. The 4 pieces are conjoined to create the outer diameter of the vessel, shown in Figure 14.

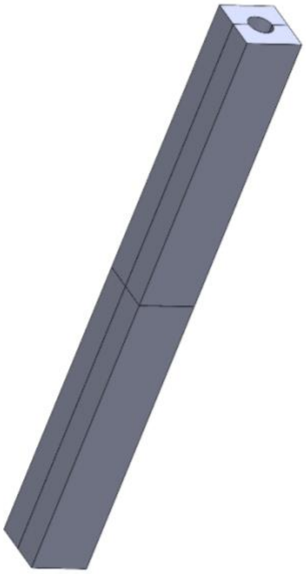

Figure 14. Assembly of Tube Mold Jig in SolidWorks

Two rectangular clamps or covers were manufactured to tighten the seal of the 4 interacting pieces which make up the vessels' outer diameter and prevent any leaking of the silicone. The top clamp is completely open on both ends, while the bottom end contains a 2" fill with a through hole for the mandrel to sit, shown in Figure 15.

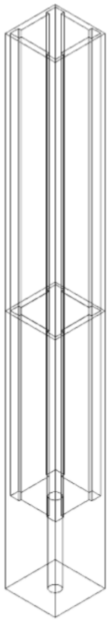

Figure 15. Assembly of Mold Clamps in SolidWorks.

The last component is a stand which allows for all pieces to remain in place and stable during the silicone pouring and the curing process, shown in Figure 17.

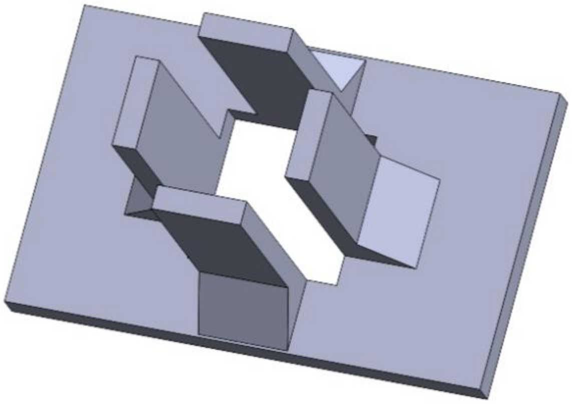

Figure 16. Tube Molding Stand in SolidWorks.

Figure 17 shows an open view of the tube mold jig encased in the rectangular clamps with one tube mold piece removed to provide visibility within the assembly.

Figure 17. Complete Silicone Artery Molding Jig.

Four mandrels were used to create the 0.25” inner diameter of the vessels with varying surface roughness for each of the 3 experimental groups. The first mandrel used was a titanium rod purchased from McMaster-Carr, shown in Figure 18 and created the smooth group of arteries with no additional surface roughness added.

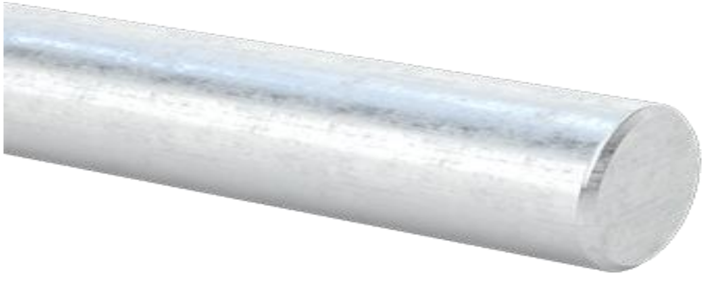

Figure 18. Polished Multipurpose Aluminum Rod for Smooth Artery Phantoms.

This smooth artery group acts as a baseline for acoustics and sound frequency for laminar and turbulent flow at different volumetric flow rates. The following mandrels were 3D-printed with hexagonal bumps created in SolidWorks using the 3D Texture tool with bump heights of 0.04” and 0.06”. Due to the volume limitation of the print bed, the mandrels were printed in two pieces and super glued together to get the desired length of the arteries, shown in Figure 19.

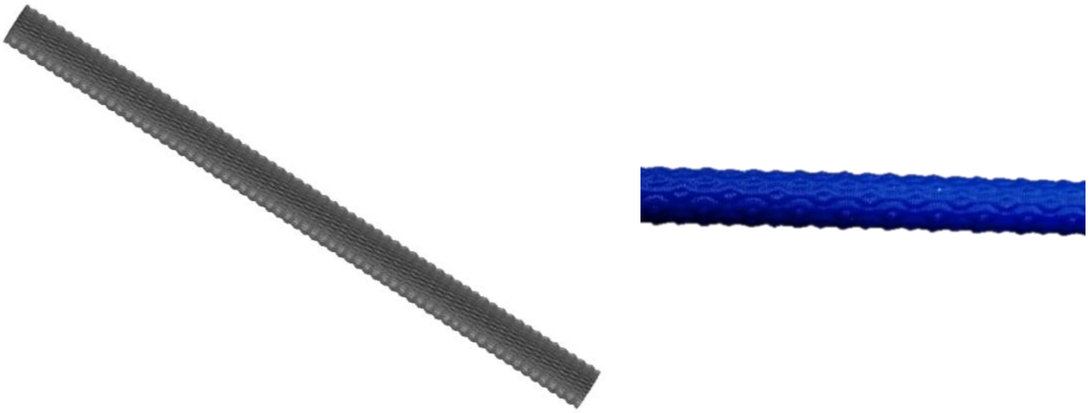

Figure 19. Roughened mandrel created in SolidWorks and 3D Printed.

DragonSkin10 NV was used to mold all 9 arteries due to its high elasticity, tensile strength, and widespread use in the biomedical industry for phantom molding. Equal amounts of the two-part silicone mold are mixed and carefully pipetted into the mold to prevent the formation of air bubbles and left to cure for approximately 75 minutes.

3.2.2 BIOPAC Contact Microphone and Data Acquisition System

The BIOPAC TSD108A piezoelectric contact microphone was used to record the sound of fluid flow through the different artery groups and is shown in Figure 20.

Figure 20. TSD108A Contact Microphone

The microphone can measure various physiological sounds such as Korotkoff sounds, rubbing or grinding, glottal activity, and muscle fiber contraction. However, in this application, the contact microphone is used in the flow-loop to measure the acoustical signature associated with the different smooth and roughened arteries. The contact microphone interfaces directly with the DA100C transducer amplifier to allow for all recorded sounds to be gathered and analyzed using the Acq*Knowledge®* software. The contact microphone measures sound data using the suggested filter settings in its technical specification sheet detailed in Appendix A. Data was acquired using 10HZ LP OFF, LP 300Hz, HP 0.05Hz, and a gain of 50.

3.2.3 Water Pump and Flowmeter

Two important components of the flow-loop system are the water pump and the flowmeter due to the impact of volumetric flow rate and fluid velocity on the Reynolds

Number and gathered sound frequencies. The water pump used was a PULACO miniature, fully-submersible, low-power pump which had a volumetric flow rate range of 0.1-1.35 L/min, shown in Figure 21.

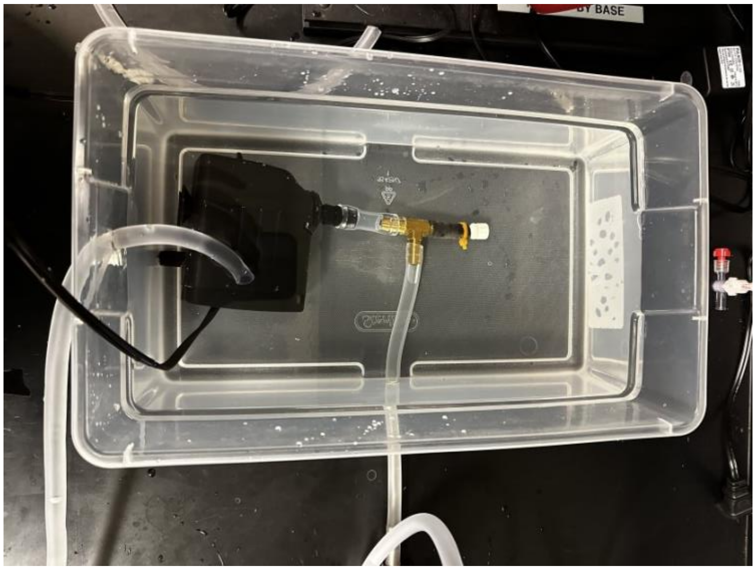

Figure 21. Submersible Water Pump in Reservoir.

Similarly, the water pump allows for the same velocities to be replicated using different artery phantoms to determine the reproducibility of the artery manufacturing method and acoustic differences between different artery test groups. An OMEGA acrylic variable flow meter was used to control flow rate of water entering the silicone artery and provide readings of flow in cubic centimeters per minute with an accuracy of ±3%, shown in Figure 22.

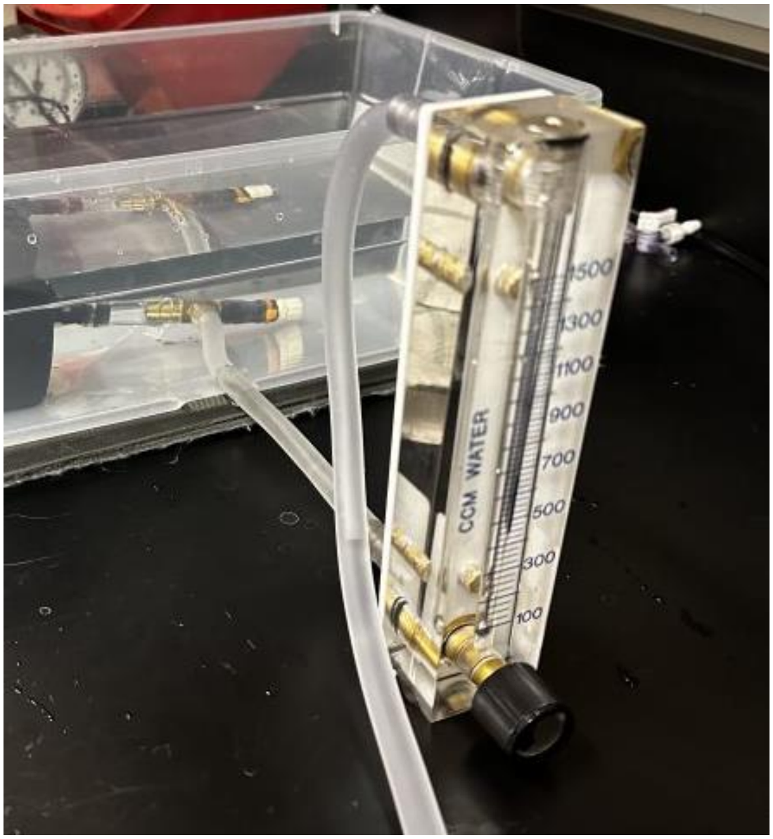

Figure 22. OMEGA Flowmeter.

The flowmeter has a range of 100-1500 CCM or 0.1-1.5 L/min and can provide readings for the full range of the water pump.

3.2.3 Pressure Transducers

In this study, two DELTRAN disposable pressure transducers (DPT-100) are used to interface with the BIOPAC MP160 and DA100C system to provide information on the pressure differences across both smooth and roughened arteries. The two DPT-100s were calibrated in the Acq*Knowledge®* software in parallel with a sphygmomanometer which generated known pressures to determine the associated voltage readings and placed at either end of the silicone phantoms in the flow loop.

3.2.4 Flow-Loop System

The flow-loop system is the interaction of the silicone phantom, contact microphone and BIOPAC acquisition system, contact microphone, water pump, flowmeter, and pressure transducers, which is all shown in a schematic diagram in Figure 23.

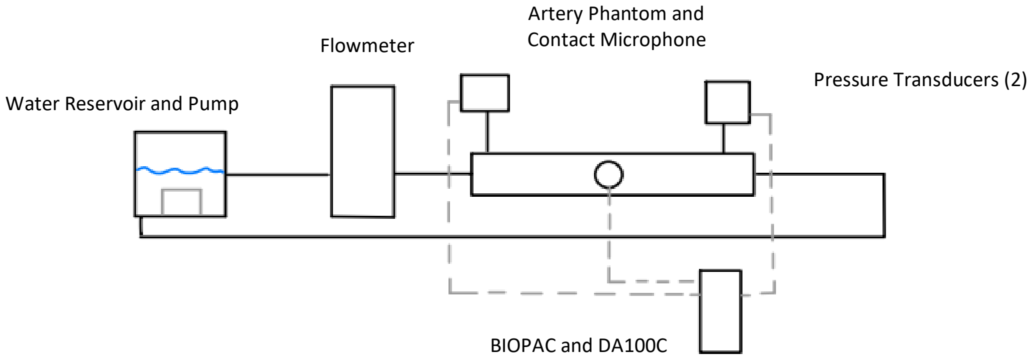

Figure 23. Schematic of Flow Loop.

The flow-loop allowed for continuous testing of a single artery using a specified flow rate or velocity of fluid from the water reservoir through the artery and the rest of the loop and back into the water reservoir. To prevent any vibrations that may contaminate the data acquisition, a sound dampening, and anti-vibration padding was placed under the water reservoir as well as under the silicone artery, shown in Figure 24.

Figure 24. Anti-Vibration Padding for Acoustic Testing

3.3 Data Analysis

Acoustic and pressure data were gathered from the flow experimental studies and analyzed using the Acq*Knowledge®* software to generate spectral graphs and determine the pressure differences across the length of each phantom. For data collection, a sampling rate of 40,000 Hz was used to ensure that the full spectral response could be captured, and aliasing of the frequency response could be prevented. With respect to the gathered sound data, digital analyzing allowed for data in the time domain to be transformed into data in the frequency domain in the form of a power spectral density graph. More specifically, power spectral density graphs (PSDs) were created for each data collection using discrete Fourier transforms embedded in the PSD function in Acq*Knowledge®*. Digital data analysis in Acq*Knowledge®* for all phantoms included applying a 60 Hz band-stop filter to remove any electrical noise interference and applying a Hanning window with a window size of 533333, overlap length of 266666, and FFT width of 524288 (2^{19}). Pressure readings from the water reservoir and both ends of the arteries were averaged to determine the head loss generated by the pump and the pressure drop for each artery. The values were applied to Bernoulli’s Equation to determine the total head loss and experimental friction factor associated with each tube. The experimental friction factor and calculated Reynolds Number were used to determine the experimental relative roughness using the Moody Diagram and compared with the measured relative roughness of the artery.

CHAPTER 4

RESULTS

The results of this experimental study show the difference of acoustic signatures between silicone phantom arteries with smooth and roughened inner diameter surfaces. Controlled flow studies were performed to determine the difference in the frequency spectrum between the various arteries with different degrees of relative roughness. The assumption of steady-state flow was used during these studies such that the data acquisition time did not play a role in the spectral results of each artery phantom. Three phantoms of each smooth and roughened inner diameter surfaces were tested to determine the difference in spectral response between a theoretical laminar and turbulent flow rate. The frequency peaks and corresponding magnitudes were used to compare waveforms associated with each artery.

4.1 Frequency Response of Flow through Smooth Artery Phantoms

Three smooth silicone artery phantoms were tested at the theoretical laminar and turbulent flow rates of 0.2 and 1.3 L/min, determined by the calculations shown in Appendix B, controlled by the Omega flowmeter. In total, each artery was tested 3 times on 3 separate occasions at the 0.2 and 1.3 L/min to determine the repeatability of the flow loop and the precision of the sound measurements.

The results of the flow studies conducted at 0.2 L/min, the theoretical laminar velocity, for the 3 smooth artery phantoms was a power spectral density graph which showed frequencies with high energy levels or peaks at approximately 12, 24, 36, and 48 Hz, shown in Figure 25.

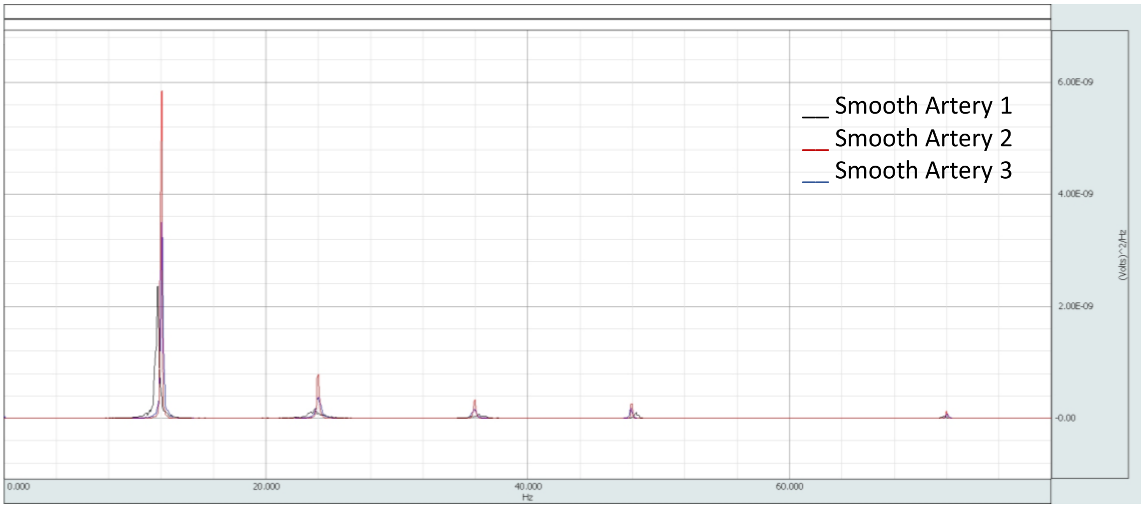

Figure 25. PSD of Smooth Arteries at 0.2 L/min.

The range of power magnitudes for each artery at each frequency varied with the largest difference being 3.49E-09 at 12 Hz. Flow across the three phantoms displayed pressure drops across the length of the tube at an average of 0.145-, 0.210-, and 0.239-mm Hg. An example of raw data sample collection is provided in Appendix C. The pressure drops across artery phantoms are displayed in Appendix D.

In contrast, at the theoretical turbulent flow rate, the 3 smooth artery phantoms displayed higher energy peaks at around 14, 29, 45, and 75 Hz, shown in Figure 26. This highlights the frequency response difference between a low and high flow rate for the same smooth phantoms.

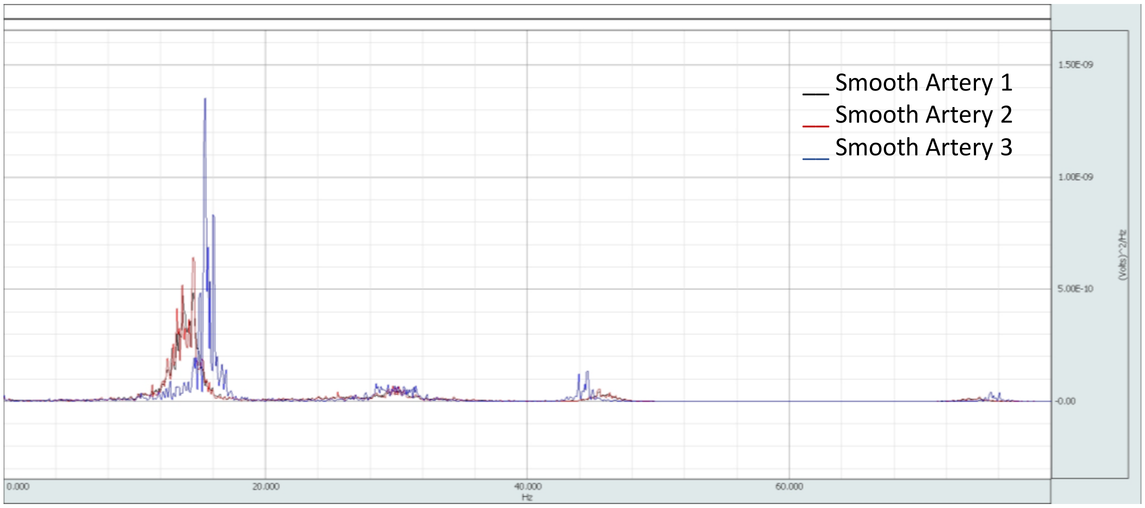

Figure 26. PSD of Smooth Arteries at 1.3 L/min.

The difference between the laminar and turbulent flow rates for smooth phantoms with respect to their spectral content is shown in their power magnitudes. More specifically, at 1.3 L/min, the differences in power magnitudes between arteries is smaller than that at the 0.2 L/min flow rate with a difference between the maximum value of each peak being 4.21E-09. Another difference is that at a laminar flow rate the phantoms showed a larger power magnitude for each frequency peak and is seen most evidently between each graph’s fundamental frequency at 12 and 14 Hz. Another difference between the two flow experiment results is the change in pressure drop across the length of each artery. At 1.3 L/min, the average pressure drop for each artery was 7.781-, 7.476, -, and 7.818 mm Hg. The differences between the two flow rates can be more clearly seen in a direct comparison of a single artery phantom, shown in Figure 27.

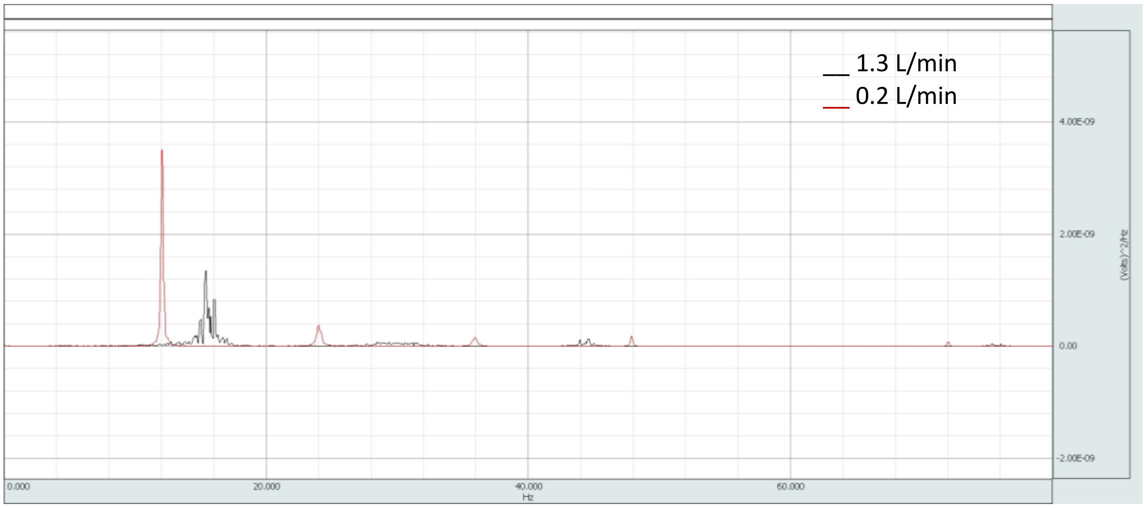

Figure 27. PSD of Smooth Artery 3 at 0.2 and 1.3 L/min.

The red waveform represents the acoustic response at the 0.2 L/min flow rate while the black waveform represents the 1.3 L/min flow rate, highlighting the shift in frequency as well as the differences in magnitude at each frequency. This comparison of a single smooth artery tested at two flow rates shows that a difference in flow behavior of a low and high Reynolds number can be detected using sound analysis. Appendix E and F display a splayed view of all three phantoms at both low and high flow rates over three experimental studies.

4.2 Frequency Response of Flow through Roughened Artery Phantoms

To compare the different acoustic responses between smooth and rough arteries, the exact experimental study was replicated using the two groups of roughened arteries. The silicone phantoms were tested at flow rates of 0.2 and 1.3 L/min, controlled by the Omega flowmeter, and using the original sampling rate and digital filtering. The two degrees of roughened arteries will be referred to as “Rough A” and “Rough B”, the A group representing the less severe degree of surface roughness on the inner diameter.

The results of the flow studies conducted for the Rough A phantom group at 0.2 L/min was a power spectral density graph which showed frequencies with high energy levels or peaks at 14, 30, 45, and 75 Hz, at power magnitudes of in the range of 1.65E-09 – 2.45E-09 V^2/Hz, shown in Figure 28.

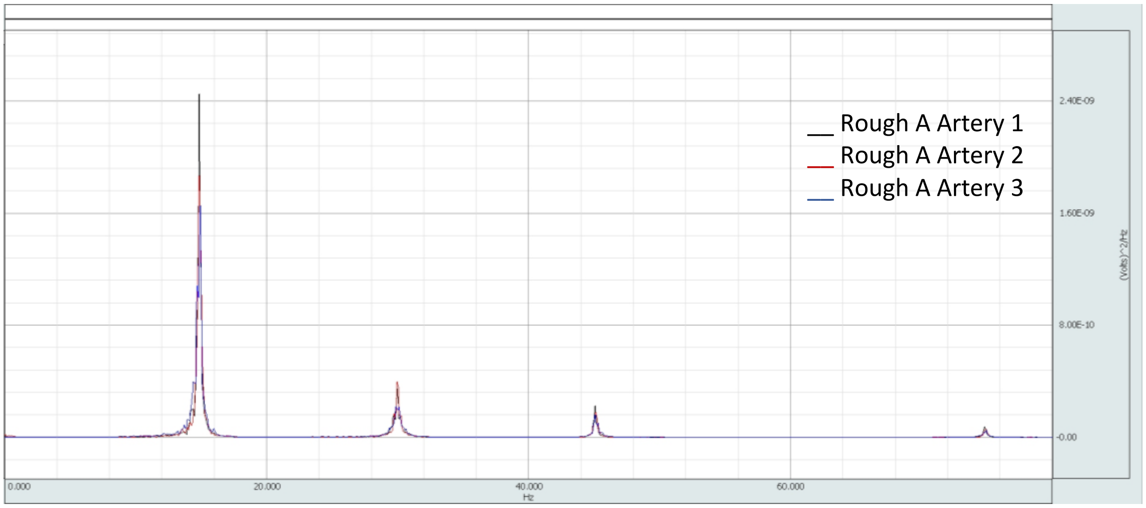

Figure 28. PSD of Rough A Arteries at 0.2 L/min.

The average pressure drop across the length of the silicone tube increased due to the added roughness on the inner diameter of the vessel when compared to the smooth arteries, summarized in Appendix D. The average pressure drop for each Rough A vessel was 0.541-, 0.422-, and 0.634 mmHg at the theoretical laminar velocity.

Unlike the changes shown between laminar and turbulent flow for the smooth artery phantoms, the Rough A phantoms showed a less dramatic difference as the frequencies with high energy remained at approximately 14, 30, 45, and 75 Hz, shown in Figure 29.

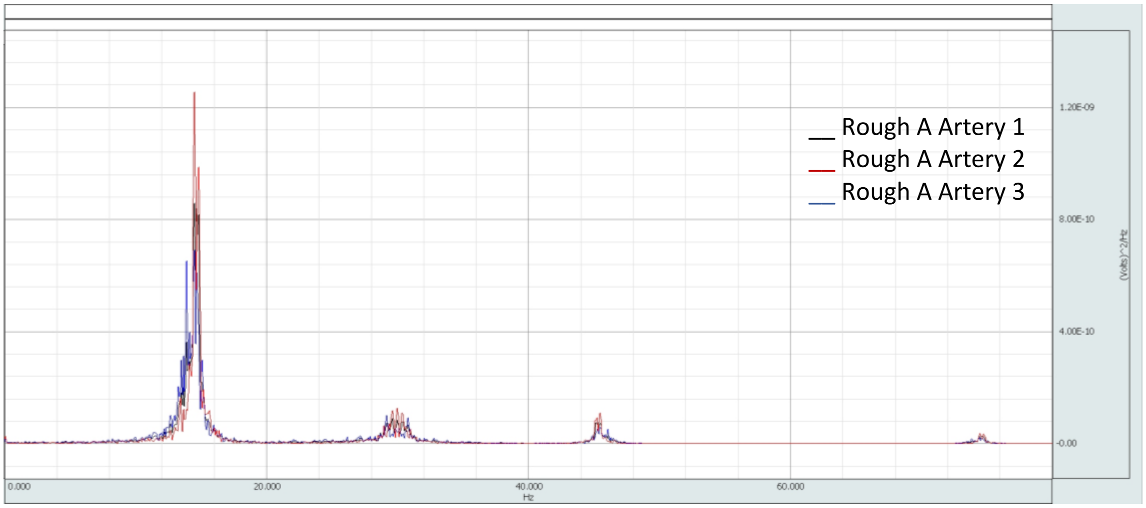

Figure 29. PSD of Rough A Arteries at 1.3 L/min.

Similar to the results of the other flow experiments performed, the magnitude difference between tubes remained relatively small, with the greatest power difference of 5.64 E-10 at 14 Hz. The average pressure drop increased by approximately 9 mm Hg, as the Rough A phantoms tested at 1.3 L/min showed an average pressure drop of 9.477-, 9.477-, 9.392 mmHg for each artery, shown in Appendix D.

A side-by-side comparison between a single Rough A phantom at 0.2 and 1.3 L/min highlights the slight variation in frequency between the low and high Reynolds number waveforms shown in Figure 30.

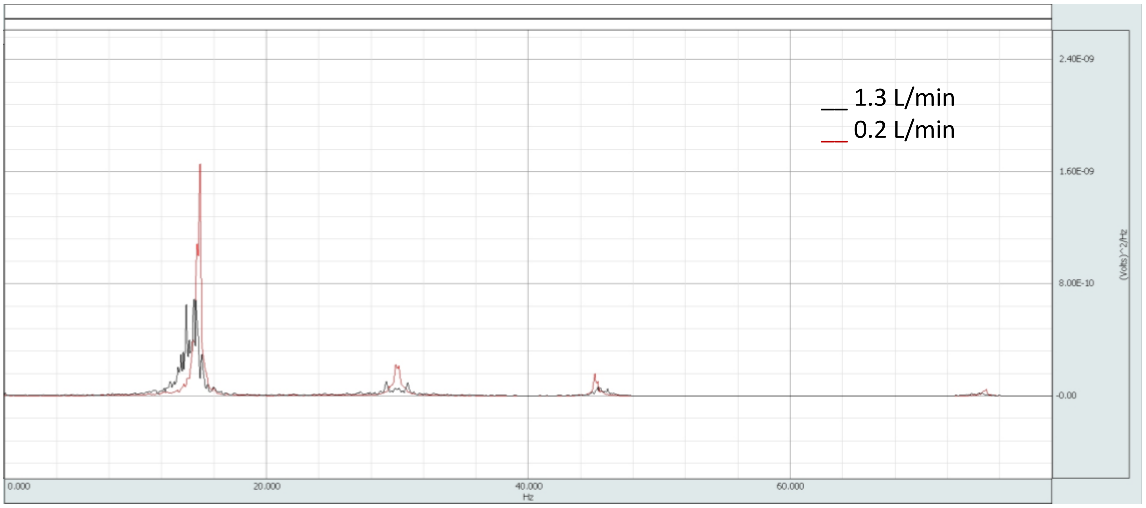

Figure 30. PSD of Rough A Artery 3 at 0.2 and 1.3 L/min.

Figure 30 highlights the difference of energy at the same frequencies with the respect to change in flow rate in the Rough A artery group. The PSD highlights the change in noise detection that emits from the fluid flow shearing on the inner diameter wall in this roughened phantom case. The results show that the sound of flow behavior at low and high Reynolds numbers for the Rough A artery example have similar peak frequency locations at 14 Hz and its harmonics. PSD graphs for each artery in the Rough A group are provided in Appendix G and H.

Similar to the PSD generated for the Rough A phantoms, the Rough B phantoms, with a higher severity of roughness, showed high spectral energy at 15, 30, 45, and 75 Hz with power magnitudes ranging from 6.04E-09-7.49E-09 V^2/Hz at a flow rate of 0.2 L/min, shown in Figure 31.

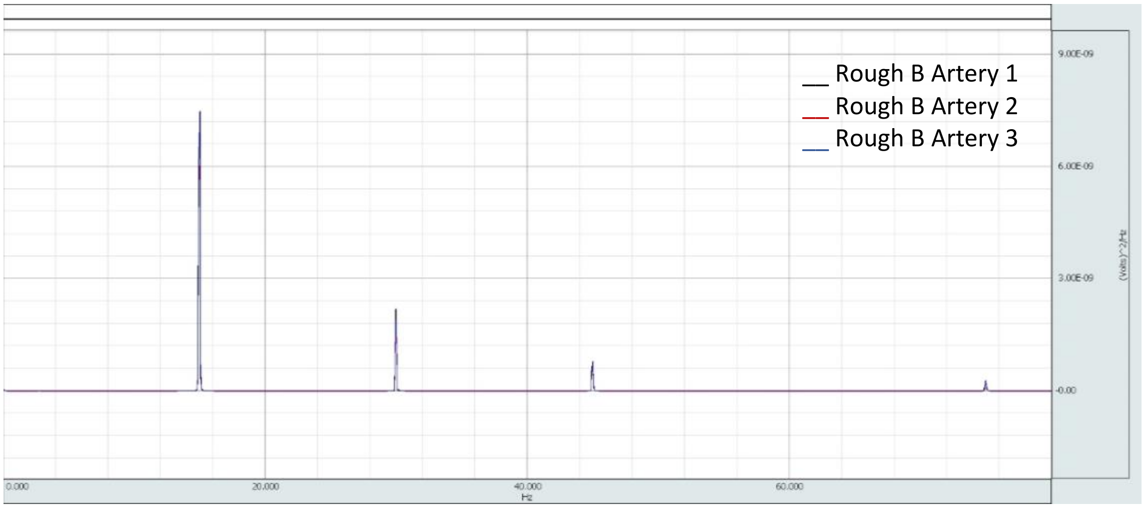

Figure 31. PSD of Rough B Arteries at 0.2 L/min.

The Rough B phantoms showed a maximum difference in power magnitudes between tubes with a value of 2.04 E-10. The average pressure drop across the roughest arteries was 1.647-, 1.359-. and 1.382 mm Hg, shown in Appendix D. The PSD of the Rough B phantoms at a flow rate of 1.3 L/min displayed energy peaks at around 16, 30, 44, 76 Hz, show in Figure 32.

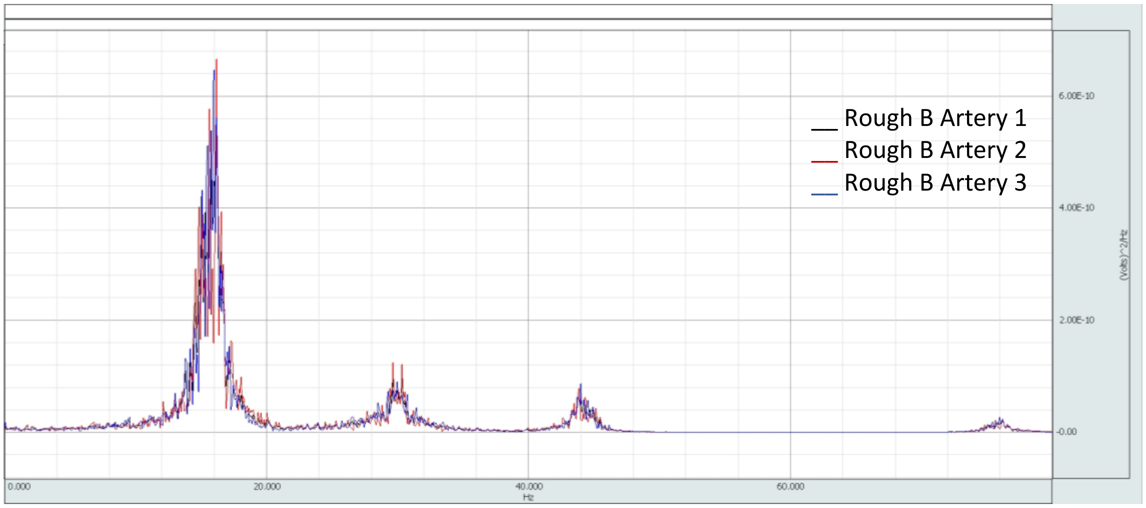

Figure 32. PSD of Rough B Arteries at 1.3 L/min.

The Rough B group had the highest power magnitude difference of 1.37E-10 at 16 Hz. Figure 33 emphasizes the absence of trends associated with a specific artery and power magnitudes. More specifically, the artery phantom that showed the largest power magnitude at 16 Hz also had the lowest power magnitude at 30 and 44 Hz.

The average pressure drop along the length of each Rough B artery phantom was 10.384, - 10.542-, and 10.464-mm Hg, shown in Appendix D which shows the positive relationship between increased roughness and loss of pressure when compared to the smooth and Rough A group. Similarly, there is also a positive relationship between the pressure drop along the length of each artery and the fluid flow rate traveling through it as well as a slight shift in frequency from 15 to 16 Hz, shown in Figure 33.

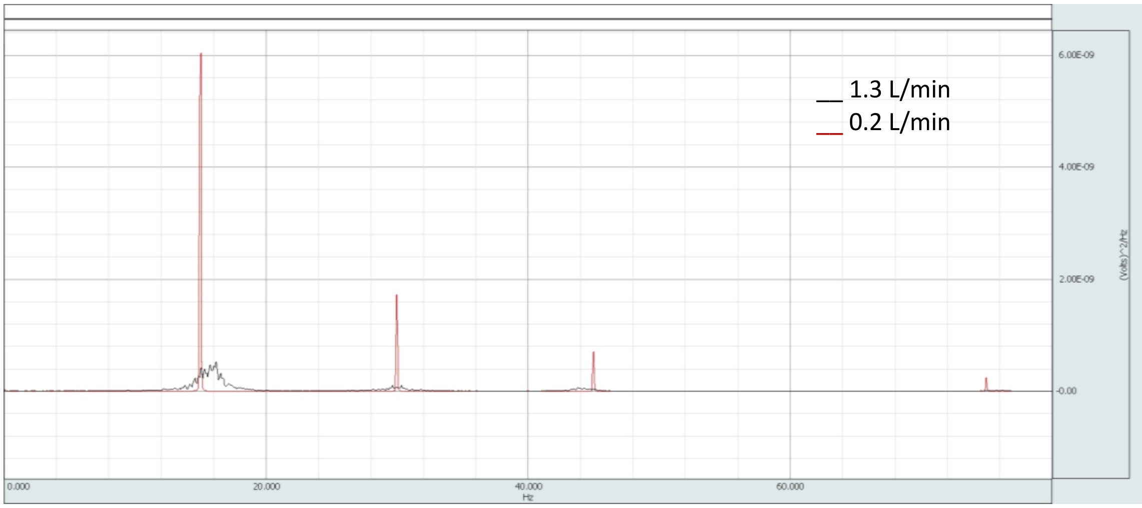

Figure 33. PSD of Rough B Artery 3 at 0.2 and 1.3 L/min.

Figure 33 depicts the difference between the same Rough B artery experiencing the theoretical laminar and turbulent flow rate traveling through it. The response of each waveform shows that at a turbulent flow rate, the first, fundamental peak shifts towards 16 Hz while, the second peak remains aligned with the laminar response, and the two following peaks experience shifts at a magnitude of 1-2 Hz. Similar to the results of flow studies performed on the smooth and Rough A phantoms, there is no obvious correlation between flow rate and the power magnitudes at the identified peaks in the Rough B group. The difference in magnitude varied for each peak when comparing the same artery at two flow rates. The repeatability of the results for the Rough B arteries are displayed as PSD graphs in Appendix I and J.

4.3 Comparison Between Smooth and Roughened Artery Phantoms

In general, there is a definitive difference between the smooth and roughened artery phantoms at both the theoretical laminar and turbulent flow rates of 0.2 L/min and 1.3 L/min, shown in Figure 34 and 35.

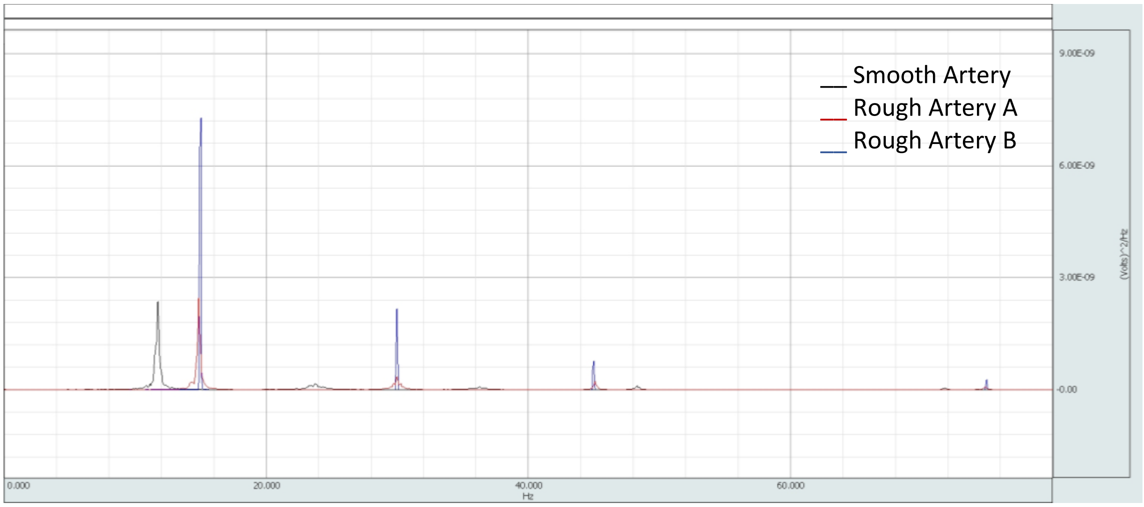

Figure 34. PSD of Smooth and Rough Arteries at 0.2 L/min.

Figure 34 displays a representative PSD comparison between the smooth, Rough A, and Rough B phantom groups at 0.2 L/min and highlights the difference in frequency peaks between the smooth and rough arteries. More specifically, there is a noticeable difference between the first frequency peak of the smooth phantoms at 12 Hz and of the rough phantoms at 15 Hz. Similarly, there was also a consistent difference between the power magnitude of the smooth and rough phantoms, such that the smooth arteries showed consistently lower power magnitudes at each of the peaks. However, the difference between the two rough groups is less obvious and the shift in frequency is smaller at the fundamental frequency from 14 to 15 Hz.

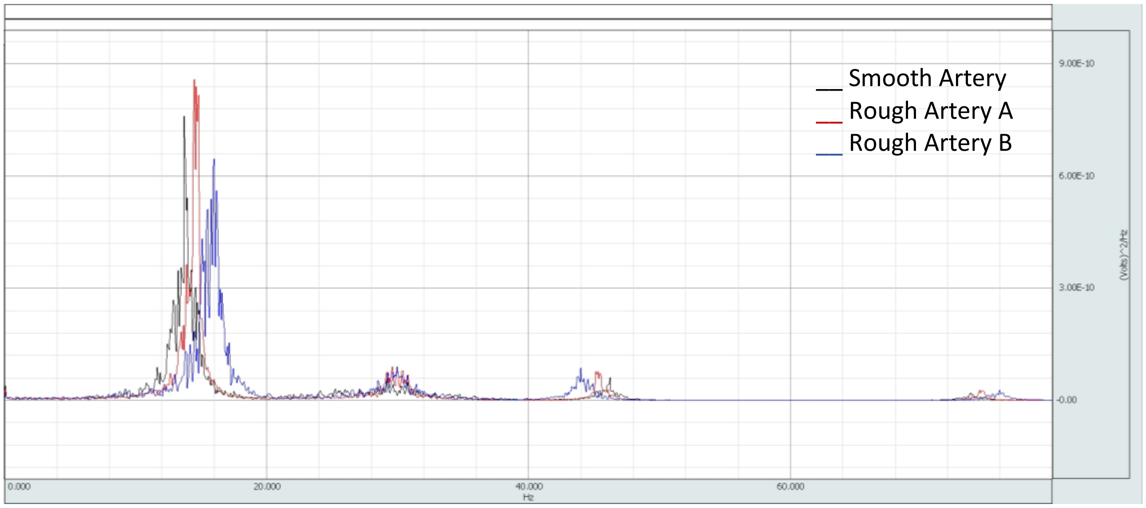

Figure 35. PSD of Smooth and Rough Arteries at 1.3 L/min

Figure 35 compares the same three artery phantoms shown in Figure 34 at a flow rate of 1.3 L/min which appear in the PSD with peaks of a wider spread less defined spread. At the theoretical turbulent flow, there is a smaller difference in frequency variation between the three phantoms as the smooth group shows a spectral response with peaks at 14 Hz and at its subsequent harmonics, while the roughened groups show a spectral response with peaks at 15-16 Hz and at its subsequent harmonics.

4.4 Moody Diagram and Friction Factor

The Moody Diagram was used to calculate the friction factor for the flow studies in which the artery phantoms experienced turbulent flow and compare the experimental relative roughness value with the measured or theoretical relative roughness. Table 1 displays a summary of the calculated friction factors for each artery phantom taken from the average pressure drop associated with each artery.

Table 1. Experimental Friction Factors for Roughened Artery Groups at 1.3 L/min

Artery Type		Experimental Friction Factor
Rough A	1	0.0701
	2	0.0701
	3	0.0694
Rough B	1	0.0770
	2	0.0782
	3	0.0776

The smooth artery phantom friction factors were calculated using Equation 11, the Blasius equation for turbulent flow in a smooth pipe, which was calculated to be 0.0206 and 0.0396, respectively, shown in Table 2.

Table 2. Theoretical Friction Factors for Smooth Arteries

Artery Type	Theoretical Friction Factor	Flow Rate [L/min]
Smooth	0.1010	0.2
	0.0396	1.3

The friction factors for turbulent flow in the Rough A and B phantoms were 0.0699 and 0.0776, respectively, and were calculated using Bernoulli's conservation of energy equation; sample equations are provided in Appendix K. Similarly, data for friction factors of each of the 3 rough arteries in the Rough A and Rough B groups are provided in Appendix L.

The relative roughness for the Rough A and Rough B phantoms were determined graphically to be approximately 0.03 and 0.037, respectively through using the calculated, experimental friction factor. Figure 36 shows an annotated version of the Moody Diagram highlighting differences in friction factor and relative roughness when the Reynolds Number is held constant.

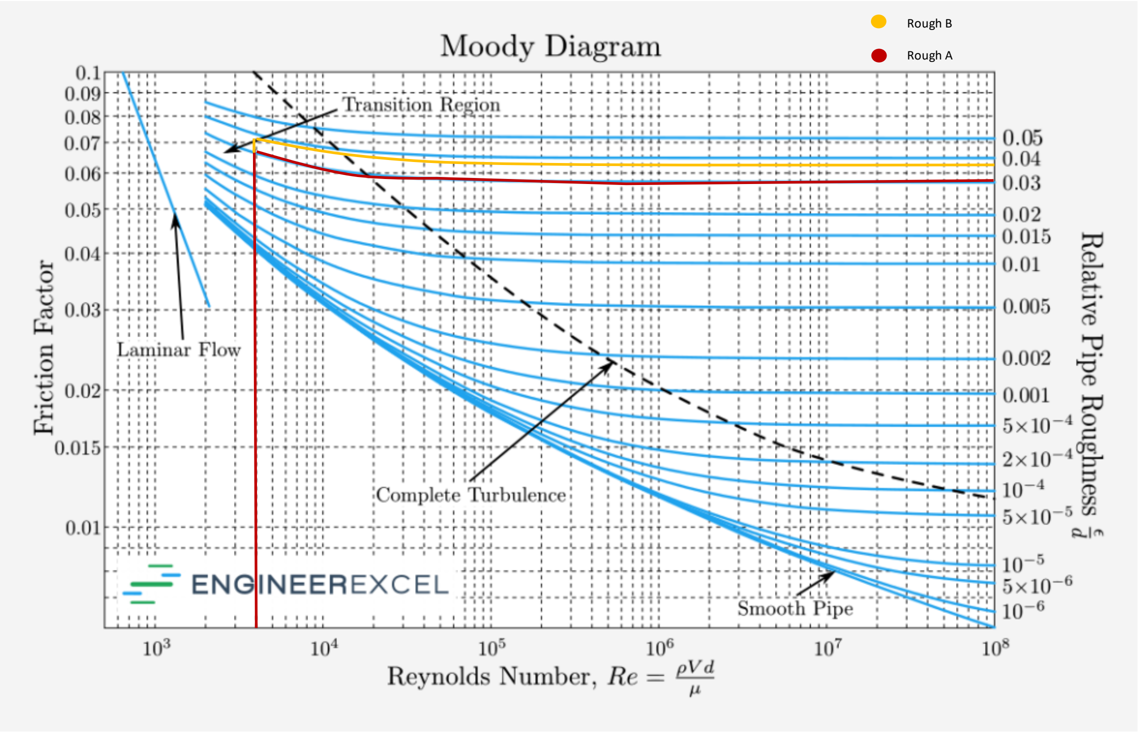

Figure 36. Annotated Moody Diagram Using Experimental Friction Factor.

CHAPTER 5

DISCUSSION

The results of the flow studies, summarized in Appendix M, comparing the acoustic response of fluid flow through a smooth artery and roughened artery which mimics inflammation of diseased vasculature show that there is a difference in spectral response between smooth and rough phantoms when tested in identical conditions. The experimental studies were conducted by collecting sound data of the smooth phantoms at a low and high Reynolds number to leverage information on the possible frequency changes that may occur due to disturbance in increased flow rates. The data gathered compared identical flow studies performed on the roughened artery phantoms to determine a possible difference in frequency between the two groups. Each of the 3 phantoms of the smooth, Rough A, and Rough B groups were compared in 3 main methods, (1) comparing a single phantom at the low and high flow rate to determine frequency changes as a function of velocity, (2) comparing a single phantom to the two others within a single group at the low and high flow rate, and (3) comparing 1 phantom from the smooth, Rough A, and Rough B to each other at the low and high flow rate. This method of sound data collection and analysis allowed for the determination of the repeatability and precision of the test method.

The results of the studies showed that there is a difference in frequency response that can be detected by the sound of fluid traveling over the surface of an elastic, silicone tube with a smooth surface and that of a roughened surface. The sound vibrations of fluid flowing through the silicone phantoms were transformed as PSD graphs and from comparing the 3 groups, there was a consistent difference between the smooth and roughened groups. A relationship between flow behavior within a phantom, the sound associated with each, and a change in the frequency response was determined by analyzing the results of the flow experiments. This is most clearly shown in the spectral differences between artery phantoms at the same flow rate as well as differences between the same arteries at different flow rates.

The studies performed at the laminar flow rate of 0.2 L/min showed that the smooth phantoms experienced spectral energy at 12 Hz and its harmonics, while the Rough A and Rough B phantoms experienced spectral energy at around 15 Hz. The results showed that peaks at a lower frequency were associated with a flow behavior that is more streamlined and representative of laminar flow while peaks at higher frequencies were associated with flow behavior that is chaotic and turbulent. The repetition of the flow experiments provides evidence for the consistency of these frequency peaks, however slight variations in magnitude were found when arteries were tested in identical conditions on different days. This suggests that the flow loop set-up as well as the artery manufacturing method may have some sources of error that result in variation. However, the power of magnitude is not reflective of the presence or absence of turbulence as it varied for each phantom within the same group and was not consistent between peaks. The result of the average pressure drops along the length of each artery phantom further supports the results of the acoustic frequency response of each group. The pressure drop increased with respect to increased roughness as the smooth, Rough A, and Rough B arteries had a change of 0.198-, 0.532-, and 1.46 mm Hg, respectively, across the length. This shows that the added roughness on the inner diameter of Rough A and B phantoms caused disturbances in the fluid flow as well as frictional losses which attributed to the difference pressure as well as in the PSD graphs at 0.2 L/min.

The flow studies performed at 1.3 L/min showed similar results suggesting that the added roughness to the inner diameter of the arteries can be detected through sound analysis. At turbulent flow rate, the frequency peaks of the smooth phantoms increased to around 14 -15 Hz and its harmonics. However, the Rough A phantom response at the high Reynolds number flow remained nearly unchanged and displayed a response with a frequency peak at around 14 Hz. This lack of frequency shift suggests that even at a low Reynolds number and slower velocity, flow through the Rough A phantoms may exhibit turbulent behavior. While the Rough B phantoms experienced a 1 Hz increase to 16 Hz without a change in its subsequent peaks when compared to the 0.2 L/min results. The similarities of the spectral peaks of the smooth arteries at 1.3 L/min and the roughened arteries at 0.2 L/min suggest that the smooth arteries are experiencing turbulent flow and changes in flow behavior similar in noise and vibration to that of the roughened phantoms at a theoretical laminar flow. Similarly, it provides a baseline for what turbulent flow looks like in a spectral graph when using theoretical calculations and rigid pipe assumptions. Due to these similarities, it is assumed that the added roughness results in disturbed, turbulent flow with increased frictional losses at both the low and high flow rates. However, there is no difference in spectral graphs between the Rough A phantoms, with the less severe degree of roughness, when comparing results at 0.2 and 1.3 L/min which suggests that there may be a threshold in which added roughness contributes to a change in frequency peak shifts. Though, the results of studies performed using Rough B phantoms showed a change in frequency peaks between the low and high Reynolds number flow rates highlighting the possibility observing more dramatic changes in spectral graphs with increased inner diameter roughness.

The result of the average pressure drops along the length of each artery phantom further supports the results of the acoustic frequency response of each group. More specifically, it shows that the added roughness on the inner diameter of Rough A and B phantoms caused disturbances in the fluid flow as well as frictional losses which attributed to the difference in PSD graphs between smooth and rough arteries as 0.2 L/min. Similarly, the result of the average pressure drops across the length of each artery phantom increased for each group when the flow rate changed from 0.2 L/min to 1.3 L/min suggesting that the theoretical turbulent flow rate was successful in creating fluctuations in velocity for the smooth and roughened arteries. As the smooth artery, Rough A, and Rough B groups showed an increase in pressure drop of 7-, 9-, and 9- mm Hg, respectively.

The results of the calculated friction factor for each of the 3 artery phantom groups show that there is a difference in frictional losses that correspond to the pressure drop for each artery. The Rough A and Rough B artery phantom groups had an average friction factor of 0.0699 and 0.0776, respectively, and a relative roughness of 0.03 and 0.037, respectively. These calculations support the assumption that the artery manufacturing process was successful in producing roughened artery phantoms that had different degrees of roughness.

CHAPTER 6

CONCLUSION

The results of this experimental study provide evidence of an acoustic detection method for determining the difference between theoretical laminar and turbulent flow in silicone artery phantoms using samples with smooth and roughened inner diameters. The difference in frequency response between a smooth and roughened artery at the same flow rate displays the ability to identify a possible difference between laminar and turbulent flow. Similarly, an increase in relative roughness of the inner diameter of a phantom has a positive relationship with an increase in pressure drop along the phantom and supports the theoretical friction factor calculation suggesting that there is a difference between the two degrees of roughness. However, further studies should be performed to investigate a higher severity of roughness with increased sample size to validate the results of this experiment.

CHAPTER 7

LIMITATIONS

The test process for determining the acoustic signature associated with different silicone phantoms had several limitations and assumptions that should be addressed to provide a full understanding of the results drawn from this experimental study. The limitations were related to the processes of artery manufacturing, data acquisition, and roughness measurement of the phantoms.

7.1 Silicone Artery Manufacturing

The limitations of the artery manufacturing process resulted in possible inconsistencies of the artery wall strength and stiffness due to the inability to replicate the time and process of pipetting silicone into the artery mold. The silicone temperament was dependent on the degree of mixing of parts A and B as well as time spent mixing and the ambient temperature of the room. The amount of time spent mixing, intensity of the mix, and increased temperature were factors that caused the silicone to cure much faster resulting in a viscous liquid pouring down the length of the artery and ultimately led to an incomplete artery mold. The viscosity of the silicone at the time of the pour also dictated the ability of air bubbles to rise to the surface and disappear. A fast cure prevented air bubbles from reaching the surface and forced bubbles to remain in the silicone creating inconsistencies in the wall thickness. The length of the artery prevented the use of a vacuum chamber as the height of the artery jig was too large for any usable chamber because of the intended use for the artery to interface with the surrogate arm. The surrogate arm originated from a bench top model for evaluating pressure cuffs created by Dr. Yong and Dr. Geddes in 1990, and iterated upon by Shane Wilsey, a previous graduate student to create compliance curves of different arteries. Similarly, the natural viscosity of the DrgaonSkin 10 NV used prevented the fabrication of an artery with a thinner wall thickness and smaller inner diameter for a more clinically relevant model.

7.2 BIOPAC Data Acquisition

The main limitation of the BIOPAC and DA100C hardware was the oscillation of input values during data acquisition. The input values for the two pressure transducers had a range of -1.86 to 4.86 V and would oscillate between those two values and 0 during the data acquisition process. During the studies, this range of values would change and oscillate between two values and zero and was noted and accounted for during the final pressure readings. However, due to the inconsistencies of the pressure readings with the system there lies a possibility of noise or oscillating input values for the contact microphone. Additional measurements such as taking readings of ambient room noise, noise of the pump, and noise of the pump running through the flow loop without the artery phantom were taken to identify potential inconsistencies between data acquisition periods. The results of these measurements showed that there were no inconsistencies during the periods of testing, but in future experiments and tests, further investigational studies should be performed to ensure that the hardware is functioning correctly.

7.3 Relative Roughness Measurements

A limitation of this experimental study was the inability to precisely determine the exact relative roughness on the inner diameter of the roughened artery phantoms due to the features of the arteries and microscopy equipment. The difficulty in determining the roughness of the arteries was due to the circular form of the sample as two ends were taken from each artery and the inner diameter of each sample was removed using an X-Acto knife. However, it was impossible to remove the inner diameter of the silicone in a manner that had a consistent thickness for each sample and thin enough such that the sample would lie flat for microscopy purposes. Similarly, removing the sample with an extremely thin thickness caused gaps and holes in the sample. Microscopy techniques such as imaging using a tabletop SEM on an angled mount and performing 3D surface configuration was one method that was previously performed; however, the same issue of thickness and flatness skewed the results. Similarly, measurement with an SEM with high resolution and improved capabilities such as imaging using 3-axis rotation was attempted. However due to the high vacuum power, DragonSkin 10 NV was not a suitable material to be placed into the SEM due to equipment safety management processes. Another measurement method was the use of a profilometer; however, the large surface roughness imprinted on the inner diameter and the elasticity of the sample made it impossible to measure.

7.4 Rigid Pipe Assumptions

This experimental study is based on fluid mechanics and governing equations that assume the artery phantoms manufactured are rigid pipes. The assumption fails to encapsulate the impact of the elasticity of the walls and the impact of movement of fluid against and along the silicone walls. However, the assumptions are used due to the limitations of analyzing the friction factor in relations to the Moody Diagram and have been deemed acceptable for the use of this analysis. However, further research and possible mathematical models could provide a more accurate representation of the artery phantoms and fluid behavior.

CHAPTER 8

FUTURE DIRECTIONS

The scope of this study was to determine a difference between laminar and turbulent flow through different artery phantoms with varying degrees of relative roughness of the inner diameter using acoustic analysis. There are several possibilities for future studies to be performed to further validate the results of this experiment through addressing the limitations and further investigating topics such as quantifying relative roughness using other measurement methods. More specifically, further studies could include additional testing using the same flow loop and manufacturing processes to create artery phantoms with an inner diameter roughness that is more severe than the Rough A and B phantoms to determine if this will result in a continuous shift of frequency peaks in the spectral graph. This may serve to provide more data and evidence that support the claim of a frequency shift between smooth and rough arteries at the theoretical laminar flow rate. Another possible study includes outsourcing compliant arteries with a known relative roughness from molding or 3D printing manufacturing companies which would allow for a more clinically relevant study as well as eliminate the need for roughness measurements of the inner diameter wall.

Improvements that could be made to the current flow loop to optimize testing for more precise data collection include implementing a digital flowmeter for more accurate readings of flow rate through the artery and a sound isolation chamber for minimizing possible external noise from contaminating the signal.

REFERENCES

[1] Semmlow, John, and Ketaki Rahalkar. “Acoustic detection of coronary artery disease.” *Annual review of biomedical engineering* vol. 9 (2007): 449-69. doi:10.1146/annurev.bioeng.9.060906.151840

[2] Palacio, Ana et al. “Social determinants of health score: does it help identify those at higher cardiovascular risk?.” *The American journal of managed care* vol. 26,10 e312-e318. 1 Oct. 2020, doi:10.37765/ajmc.2020.88504

[3] Weissgerber, Tracey L. “Flow-mediated dilation: can new approaches provide greater mechanistic insight into vascular dysfunction in preeclampsia and other diseases?.” *Current hypertension reports* vol. 16,11 (2014): 487. doi:10.1007/s11906-014-0487-z

[4] “Project Risk Reduction by Therapy.” *ASCVD Risk Estimator +*, tools.acc.org/ascvd-risk-estimator-plus/#!/calculate/estimate/.

[5] Toth, P P. “Subclinical atherosclerosis: what it is, what it means and what we can do about it.” *International journal of clinical practice* vol. 62,8 (2008): 1246-54. doi:10.1111/j.1742-1241.2008.01804.x

[6] Libby, Peter et al. “Atherosclerosis.” *Nature reviews. Disease primers* vol. 5,1 56. 16 Aug. 2019, doi:10.1038/s41572-019-0106-z

[7] Ross, R. “Atherosclerosis--an inflammatory disease.” *The New England journal of medicine* vol. 340,2 (1999): 115-26. doi:10.1056/NEJM199901143400207

[8] Jebari-Benslaiman, Shifa et al. "Pathophysiology of Atherosclerosis." *International journal of molecular sciences* vol. 23,6 3346. 20 Mar. 2022, doi:10.3390/ijms23063346

[9] Akers, Emma J et al. "Plaque Calcification: Do Lipoproteins Have a Role?." *Arteriosclerosis, thrombosis, and vascular biology* vol. 39,10 (2019): 1902-1910. doi:10.1161/ATVBAHA.119.311574

[10] Shioi, Atsushi, and Yuji Ikari. "Plaque Calcification During Atherosclerosis Progression and Regression." *Journal of atherosclerosis and thrombosis* vol. 25,4 (2018): 294-303. doi:10.5551/jat.RV17020

[11] "Coronary Angiogram." *Mayo Clinic*, Mayo Foundation for Medical Education and Research, 14 Dec. 2021, www.mayoclinic.org/tests-procedures/coronary-angiogram/about/pac-20384904.

[12] Achenbach, Stephan. "Coronary CT angiography-future directions." *Cardiovascular diagnosis and therapy* vol. 7,5 (2017): 432-438. doi:10.21037/cdt.2017.06.10

[13] Eckert, Joachim et al. "Coronary CT angiography in managing atherosclerosis." *International journal of molecular sciences* vol. 16,2 3740-56. 9 Feb. 2015, doi:10.3390/ijms16023740

[14] Willeit, Peter et al. "Carotid Intima-Media Thickness Progression as Surrogate Marker for Cardiovascular Risk: Meta-Analysis of 119 Clinical Trials Involving 100 667 Patients." *Circulation* vol. 142,7 (2020): 621-642. doi:10.1161/CIRCULATIONAHA.120.046361

[15] Lorenz, Matthias W et al. “Prediction of clinical cardiovascular events with carotid intima-media thickness: a systematic review and meta-analysis.” *Circulation* vol. 115,4 (2007): 459-67. doi:10.1161/CIRCULATIONAHA.106.628875

[16] Gaarder, Mario, and Therese Seierstad. “Measurements of carotid intima media thickness in non-invasive high-frequency ultrasound images: the effect of dynamic range setting.” *Cardiovascular ultrasound* vol. 13 5. 27 Jan. 2015, doi:10.1186/1476-7120-13-5

[17] Poredoš, Pavel, and Mateja Kaja Ježovnik. “Markers of preclinical atherosclerosis and their clinical relevance.” *VASA. Zeitschrift fur Gefasskrankheiten* vol. 44,4 (2015): 247-56. doi:10.1024/0301-1526/a000439

[18] Peters, Sanne A E, and Michiel L Bots. “Carotid intima-media thickness studies: study design and data analysis.” *Journal of stroke* vol. 15,1 (2013): 38-48. doi:10.5853/jos.2013.15.1.38

[19] Münzel, Thomas et al. “Pathophysiology, diagnosis and prognostic implications of endothelial dysfunction.” *Annals of medicine* vol. 40,3 (2008): 180-96. doi:10.1080/07853890701854702

[20] Esper, Ricardo J et al. “Endothelial dysfunction: a comprehensive appraisal.” *Cardiovascular diabetology* vol. 5 4. 23 Feb. 2006, doi:10.1186/1475-2840-5-4

[21] Onyewu, S.C., Coombs, A.T., Kromah, F. (2021). Vascular Endothelial Dysfunction and Inflammatory States. In: Scher, C.S., Kaye, A.D., Liu, H., Perelman, S., Leavitt, S. (eds) Essentials of Blood Product Management in Anesthesia Practice. Springer, Cham. https://doi.org/10.1007/978-3-030-59295-0_22

[22] Farah, Charlotte et al. "Nitric oxide signalling in cardiovascular health and disease." *Nature reviews. Cardiology* vol. 15,5 (2018): 292-316. doi:10.1038/nrcardio.2017.224

[23] Förstermann, Ulri ch, and William C Sessa. "Nitric oxide synthases: regulation and function." *European heart journal* vol. 33,7 (2012): 829-37, 837a-837d. doi:10.1093/eurheartj/ehr304

[24] Farah, Charlotte et al. "Nitric oxide signalling in cardiovascular health and disease." *Nature reviews. Cardiology* vol. 15,5 (2018): 292-316. doi:10.1038/nrcardio.2017.224

[25] Givertz, M M. "Manipulation of the renin-angiotensin system." *Circulation* vol. 104,5 (2001): E14-8. doi:10.1161/hc3001.094733

[26] Rajendran, Peramaiyan et al. "The vascular endothelium and human diseases." *International journal of biological sciences* vol. 9,10 1057-69. 9 Nov. 2013, doi:10.7150/ijbs.7502

[27] Peghaire, C et al. "The transcription factor ERG regulates a low shear stress-induced anti-thrombotic pathway in the microvasculature." *Nature communications* vol. 10,1 5014. 1 Nov. 2019, doi:10.1038/s41467-019-12897-w

[28] Yoshizumi, Masanori et al. “Stress and vascular responses: atheroprotective effect of laminar fluid shear stress in endothelial cells: possible role of mitogen-activated protein kinases.” *Journal of pharmacological sciences* vol. 91,3 (2003): 172-6. doi:10.1254/jphs.91.172

[29] Martin, Fiona A et al. “Thrombomodulin and the vascular endothelium: insights into functional, regulatory, and therapeutic aspects.” *American journal of physiology. Heart and circulatory physiology* vol. 304,12 (2013): H1585-97. doi:10.1152/ajpheart.00096.2013

[30] Park, Sang Woo et al. “Impact of endothelium roughness on blood flow.” *Journal of theoretical biology* vol. 300 (2012): 152-60. doi:10.1016/j.jtbi.2012.01.017

[31] Davies, P F et al. “Turbulent fluid shear stress induces vascular endothelial cell turnover in vitro.” *Proceedings of the National Academy of Sciences of the United States of America* vol. 83,7 (1986): 2114-7. doi:10.1073/pnas.83.7.2114

[32] Raitakari, O T, and D S Celermajer. “Flow-mediated dilatation.” *British journal of clinical pharmacology* vol. 50,5 (2000): 397-404. doi:10.1046/j.1365-2125.2000.00277.x

[33] Ma, Tianxiang et al. “Flow-mediated dilation analysis coupled with nitric oxide transport to enhance the assessment of endothelial function.” *Journal of applied physiology (Bethesda, Md. : 1985)* vol. 131,1 (2021): 1-14. doi:10.1152/japplphysiol.00039.2021

[34] Menon, E. Shashi. *Transmission Pipeline Calculations and Simulations Manual*. Elsevier/Gulf Professional, 2015.

[35] Pritchard, Phillip J., et al. *Fox and McDonald's Introduction to Fluid Mechanics, 9th Edition*. Wiley, 2015.

[36] Charlie Young, P.E. "Moody Chart for Estimating Friction Factors." *EngineerExcel*, 13 Jan. 2022, engineerexcel.com/moody-chart/.

[37] "How Do We Hear?" *National Institute of Deafness and Other Communication Disorders*, U.S. Department of Health and Human Services, www.nidcd.nih.gov/health/how-do-we-hear#:~:text=Sound%20waves%20enter%20the%20outer,malleus%2C%20incus%2C%20and%20stapes.

[38] Mcnames, James & Crespo, Cristina & Aboy, Mateo & Bassale, J. & Jenkins, L. & Goldstein, Brahm. (2002). Harmonic Spectrogram for the Analysis of Semi-periodic Physiologic Signals. 1. 143 - 144 vol.1. 10.1109/IEMBS.2002.1134427.

Yazicioglu, Yigit et al. "Acoustic radiation from a fluid-filled, subsurface vascular tube with internal turbulent flow due to a constriction." *The Journal of the Acoustical Society of America* vol. 118,2 (2005): 1193-209. doi:10.1121/1.1953267

[39] Lees, R S, and C F Dewey Jr. "Phonoangiography: a new noninvasive diagnostic method for studying arterial disease." Proceedings of the National Academy of Sciences of the United States of America vol. 67,2 (1970): 935-42. doi:10.1073/pnas.67.2.935

[40] Kim, B M, and W H Corcoran. “Experimental measurements of turbulence spectra distal to stenoses.” *Journal of biomechanics* vol. 7,4 (1974): 335-42. doi:10.1016/0021-9290(74)90028-1

[41] Akay, Y M et al. “Dynamics of the sounds caused by partially occluded femoral arteries in dogs.” *Annals of biomedical engineering* vol. 22,5 (1994): 493-500. doi:10.1007/BF02367085

APPENDICES

Appendix A. Contact Microphone Technical Specification Sheet

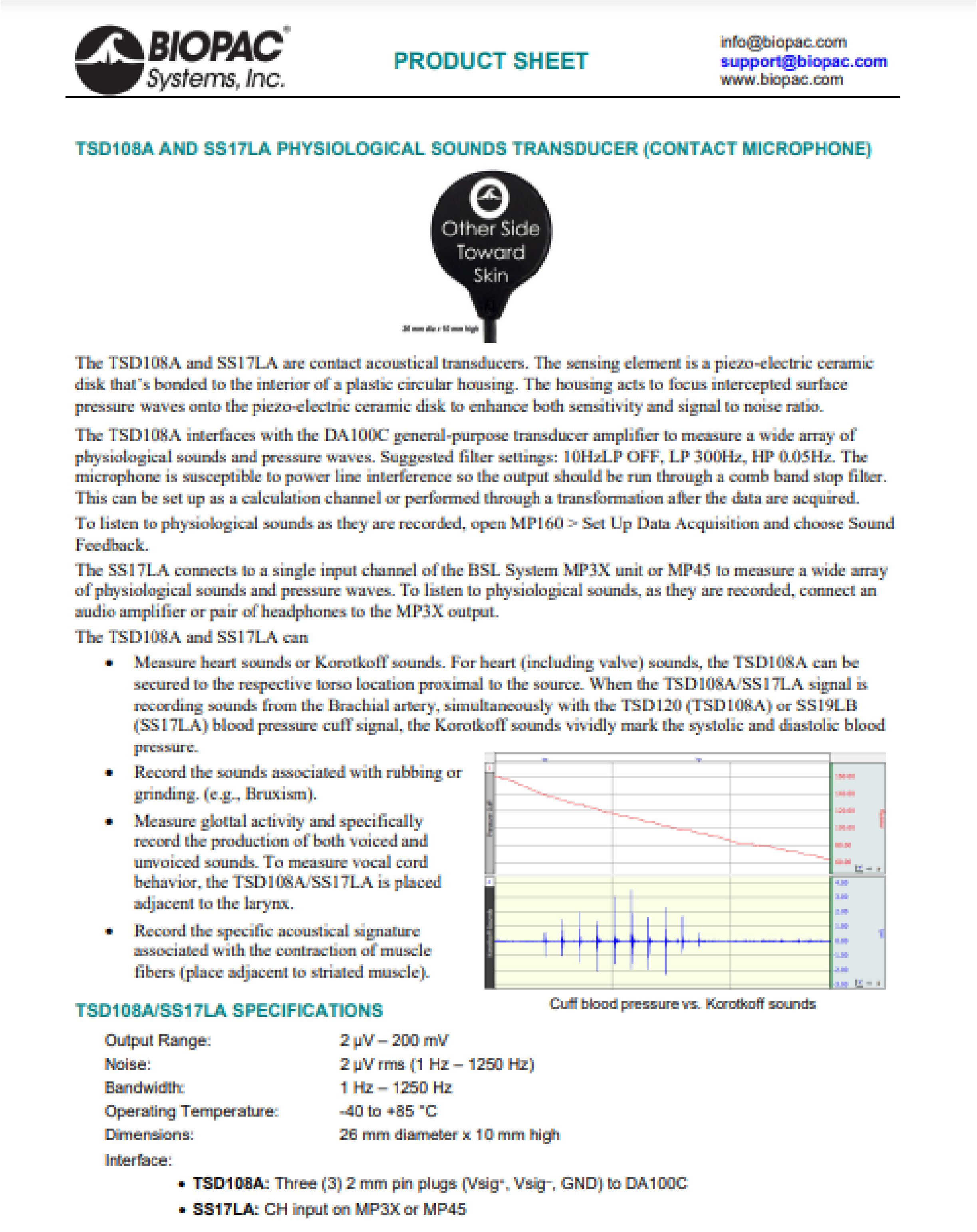

BIOPAC Systems, Inc. PRODUCT SHEET

info@biopac.com
support@biopac.com
www.biopac.com

TSD108A AND SS17LA PHYSIOLOGICAL SOUNDS TRANSDUCER (CONTACT MICROPHONE)

The TSD108A and SS17LA are contact acoustical transducers. The sensing element is a piezo-electric ceramic disk that's bonded to the interior of a plastic circular housing. The housing acts to focus intercepted surface pressure waves onto the piezo-electric ceramic disk to enhance both sensitivity and signal to noise ratio.

The TSD108A interfaces with the DA100C general-purpose transducer amplifier to measure a wide array of physiological sounds and pressure waves. Suggested filter settings: 10HzLP OFF, LP 300Hz, HP 0.05Hz. The microphone is susceptible to power line interference so the output should be run through a comb band stop filter. This can be set up as a calculation channel or performed through a transformation after the data are acquired.

To listen to physiological sounds as they are recorded, open MP160 > Set Up Data Acquisition and choose Sound Feedback.

The SS17LA connects to a single input channel of the BSL System MP3X unit or MP45 to measure a wide array of physiological sounds and pressure waves. To listen to physiological sounds, as they are recorded, connect an audio amplifier or pair of headphones to the MP3X output.

The TSD108A and SS17LA can

- Measure heart sounds or Korotkoff sounds. For heart (including valve) sounds, the TSD108A can be secured to the respective torso location proximal to the source. When the TSD108A/SS17LA signal is recording sounds from the Brachial artery, simultaneously with the TSD120 (TSD108A) or SS19LB (SS17LA) blood pressure cuff signal, the Korotkoff sounds vividly mark the systolic and diastolic blood pressure.
- Record the sounds associated with rubbing or grinding. (e.g., Bruxism).
- Measure glottal activity and specifically record the production of both voiced and unvoiced sounds. To measure vocal cord behavior, the TSD108A/SS17LA is placed adjacent to the larynx.
- Record the specific acoustical signature associated with the contraction of muscle fibers (place adjacent to striated muscle).

Cuff blood pressure vs. Korotkoff sounds

TSD108A/SS17LA SPECIFICATIONS

Output Range:	2 µV – 200 mV
Noise:	2 µV rms (1 Hz – 1250 Hz)
Bandwidth:	1 Hz – 1250 Hz
Operating Temperature:	-40 to +85 °C
Dimensions:	26 mm diameter x 10 mm high

Interface:

- **TSD108A:** Three (3) 2 mm pin plugs (Vsig+, Vsig−, GND) to DA100C
- **SS17LA:** CH input on MP3X or MP45

Appendix B. Theoretical Calculations for Laminar and Turbulent Flow Rate

$Re_{Laminar} \leq 2300$

Re = $\frac{\rho\ V\ D}{\mu}$; ρ = 997 kg/m^3, D = 0.00635 m, μ = 0.0010518

V_{MAX} [m/s] = $\frac{Re\ \mu}{\rho\ D}$= 0.3821; Any velocity under this value will be considered laminar

Q_{MIN} [m^3/s] of pump = 0.2 L/min or 3.33E-06 m^3/s

V = $\frac{Q}{CSA}$; CSA = cross-sectional area of ID = 3.165 m^2

$V_{Pump\ MIN}$ = 0.1053 m/s < 0.3821

Re = 633.87

$Re_{Turbulent}$ > 3500

V_{MAX} [m/s] = $\frac{Re\ \mu}{\rho\ D}$= 0.5815; Any velocity over this value will be considered turbulent

Q_{MAX} [m^3/s] of pump = 1.3 L/min or 2.13E-05 m^3/s

V = $\frac{Q}{CSA}$; CSA = cross-sectional area of ID = 3.165 m^2

$V_{Pump\ MAX}$ = 0.6740 m/s < 0.5815

Re = 4056.75

Appendix C. Raw Data Example from BIOPAC Data Acquisition

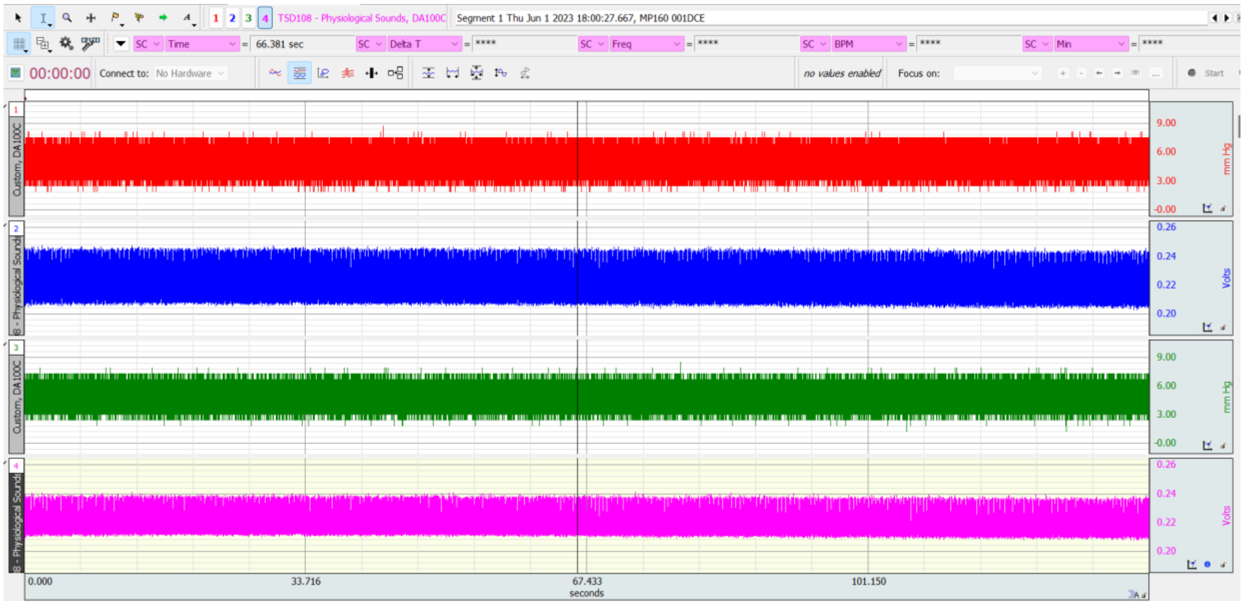

Laminar Flow Rate 0.2 L/min

Artery Group		Pressure Drop [mm Hg]			
		Trial 1	Trial 2	Trial 3	Average
Smooth	1	0.1420	0.1452	0.1493	0.1455
	2	0.2070	0.1998	0.2232	0.2100
	3	0.2490	0.2149	0.2531	0.2390
Rough A	1	0.5830	0.4779	0.5621	0.5410
	2	0.4370	0.3982	0.4308	0.4220
	3	0.6420	0.6210	0.6390	0.6340
Rough B	1	1.6550	1.6400	1.6460	1.6470
	2	1.4200	1.3700	1.2870	1.3590
	3	1.4240	1.4550	1.2670	1.3820

Turbulent Flow Rate: 1.3 L/min

Artery Group		Pressure Drop [mm Hg]			
		Trial 1	Trial 2	Trial 3	Average
Smooth	1	7.425	7.234	8.684	7.781
	2	7.342	7.420	7.666	7.476
	3	7.728	7.742	7.984	7.818
Rough A	1	9.456	9.534	9.442	9.477
	2	9.240	9.369	9.823	9.477
	3	9.452	9.230	9.495	9.392
Rough B	1	10.329	10.593	10.230	10.384
	2	10.438	10.864	10.324	10.542
	3	10.482	10.675	10.234	10.464

Appendix E. PSD of Smooth Arteries at 0.2 L/min

____ Trial 1

____ Trial 2

____ Trial 3

Smooth Artery 1

A. Overlayed View

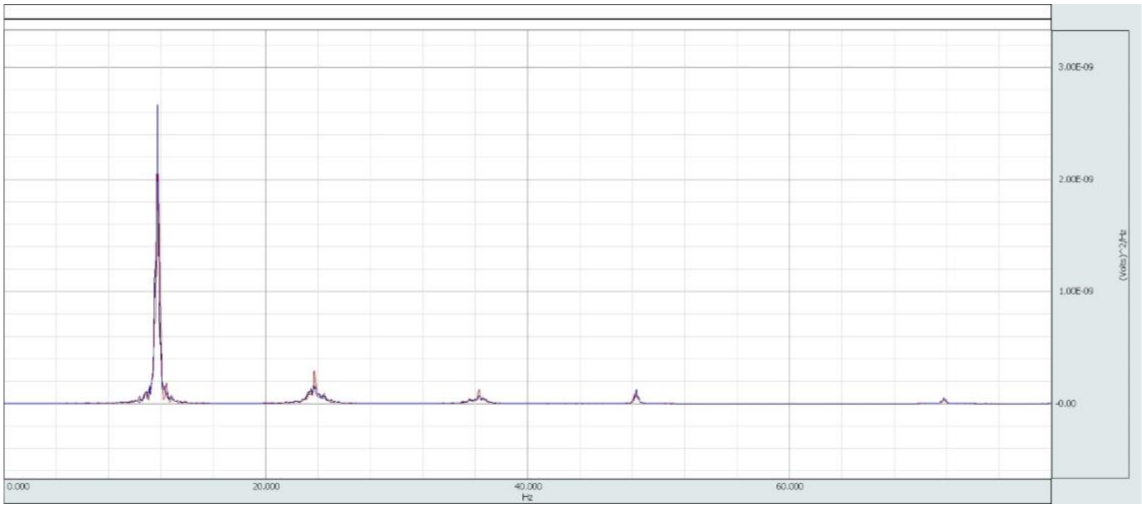

B. Splayed View

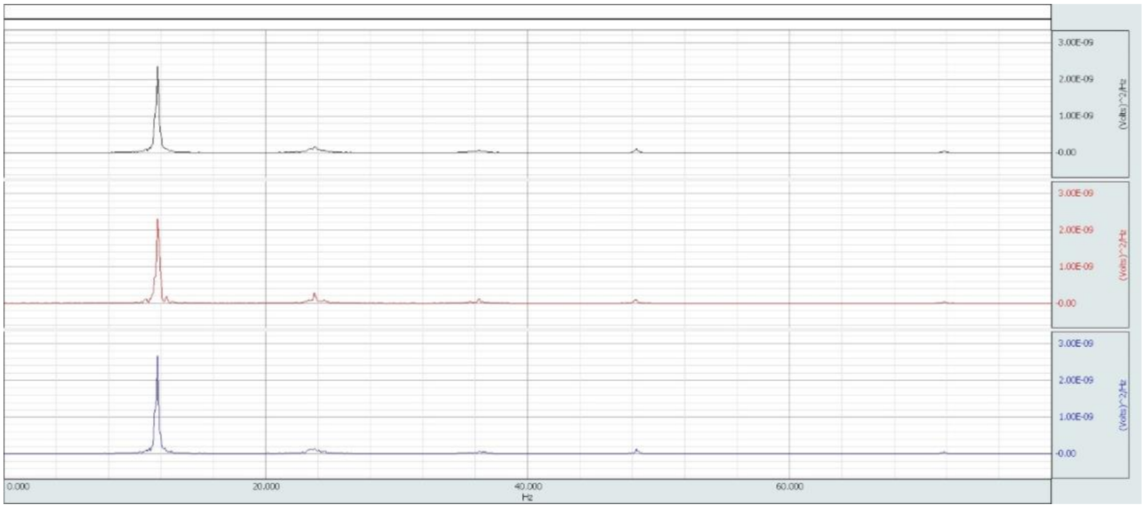

Smooth Artery 2

A. Overlayed View

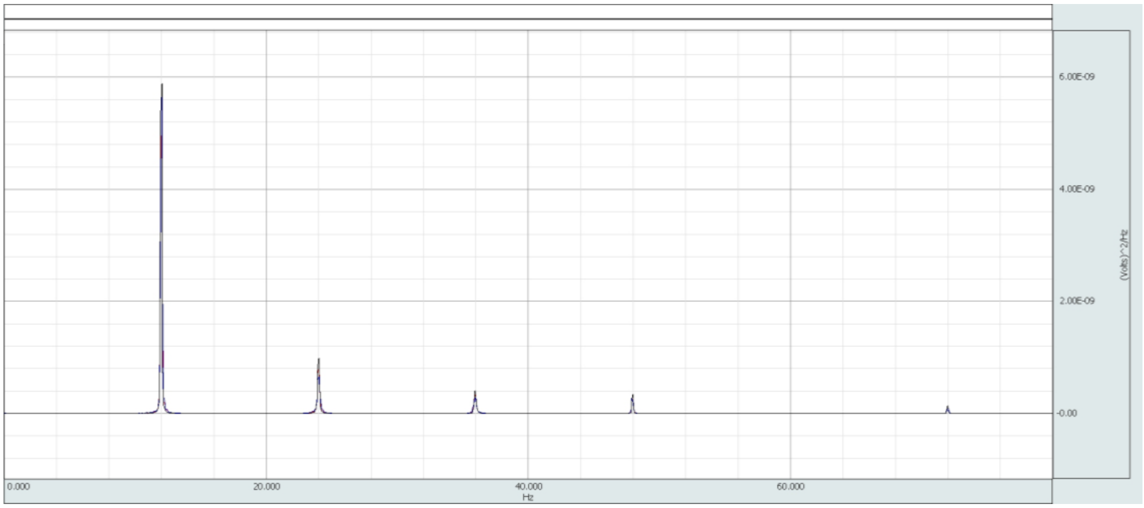

B. Splayed View

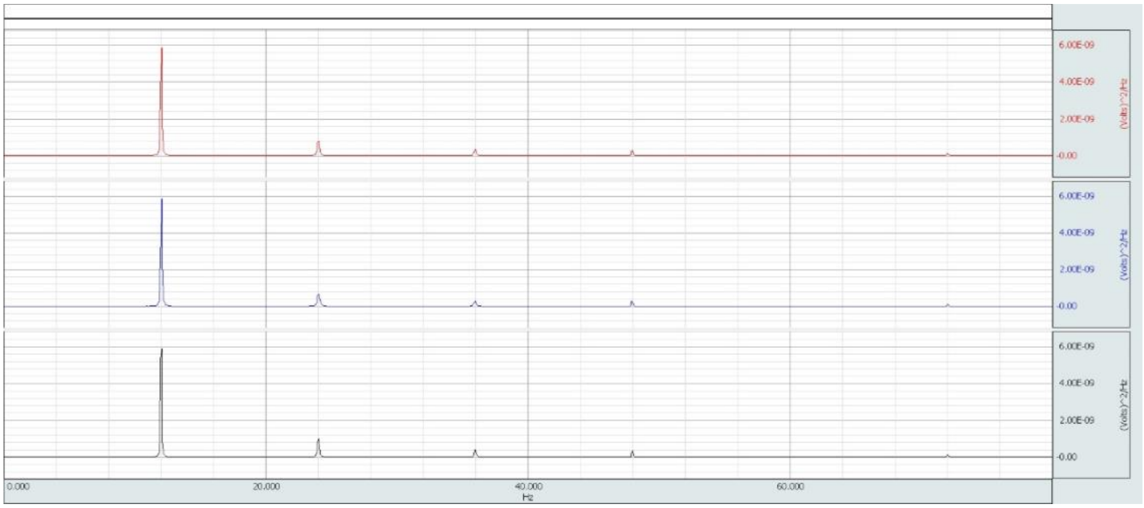

Smooth Artery 3

A. Overlayed View

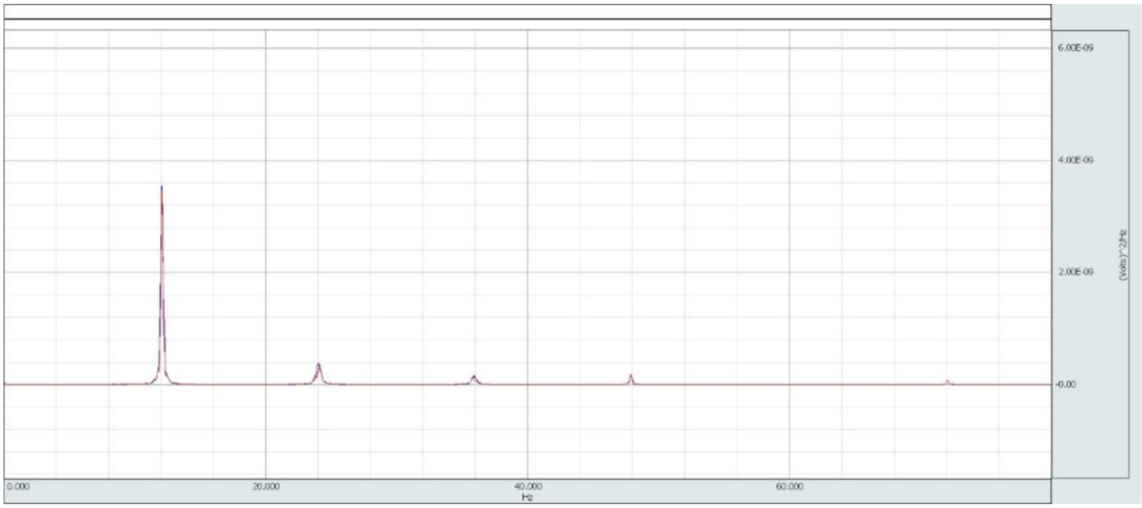

B. Splayed View

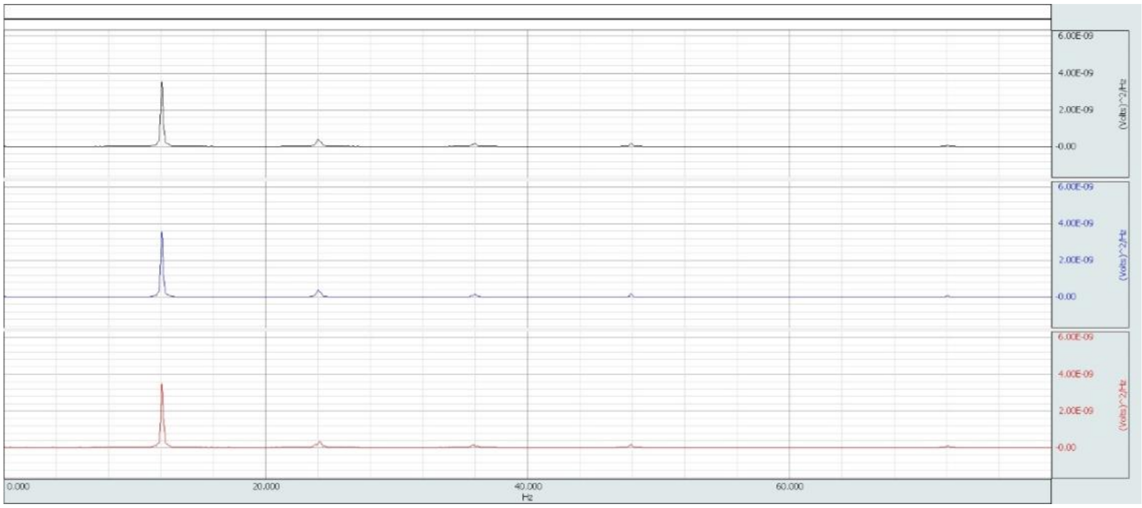

Appendix F. PSD of Smooth Arteries at 1.3 L/min

____ Trial 1

____ Trial 2

____ Trial 3

Smooth Artery 1

A. Overlayed View

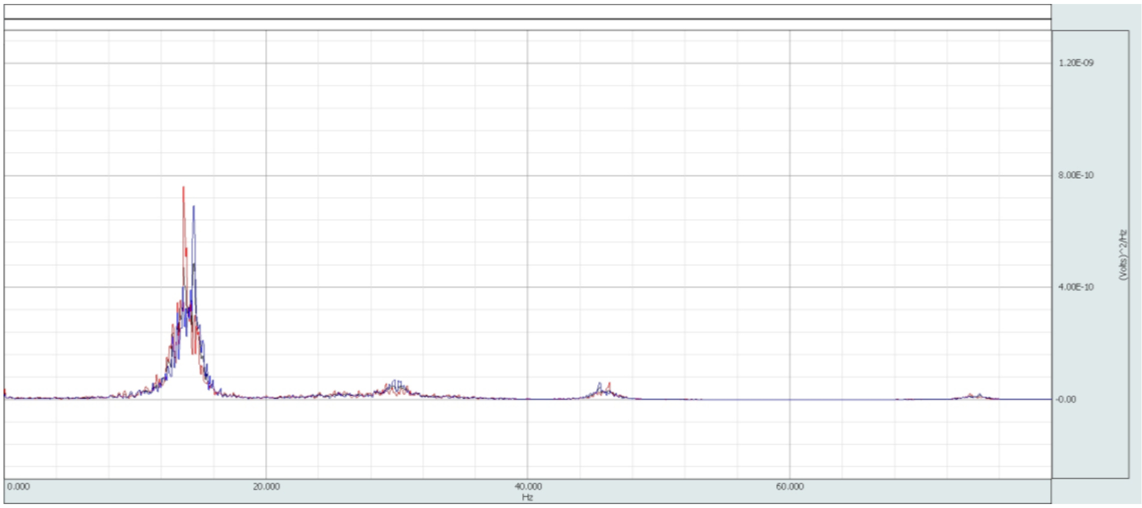

B. Splayed View

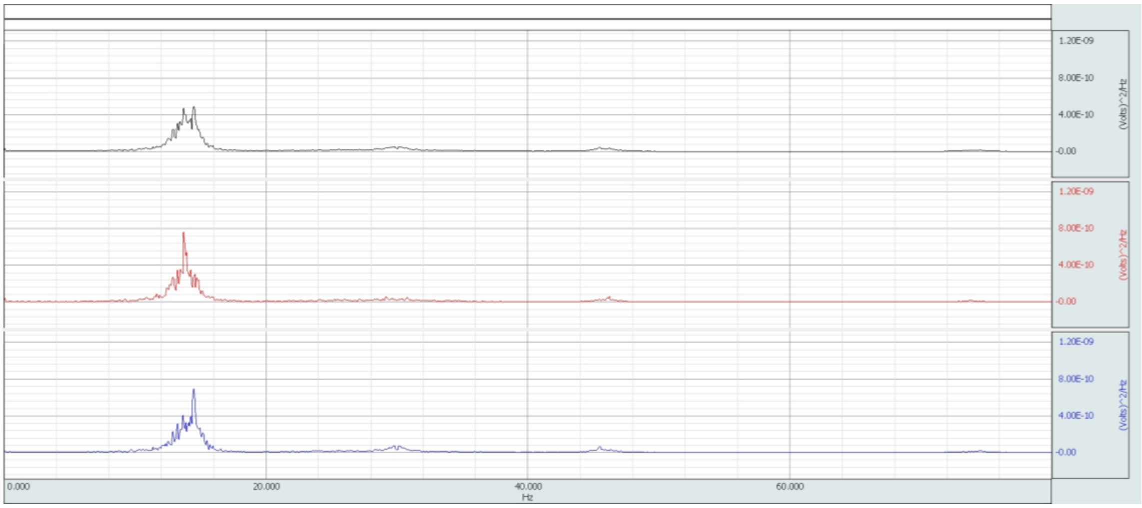

Smooth Artery 2

A. Overlayed View

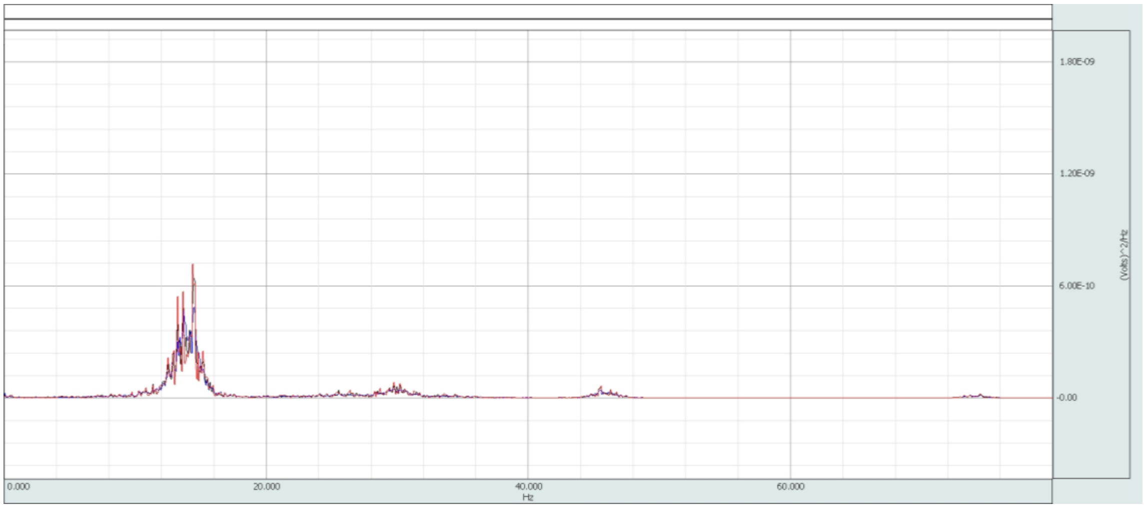

B. Splayed View

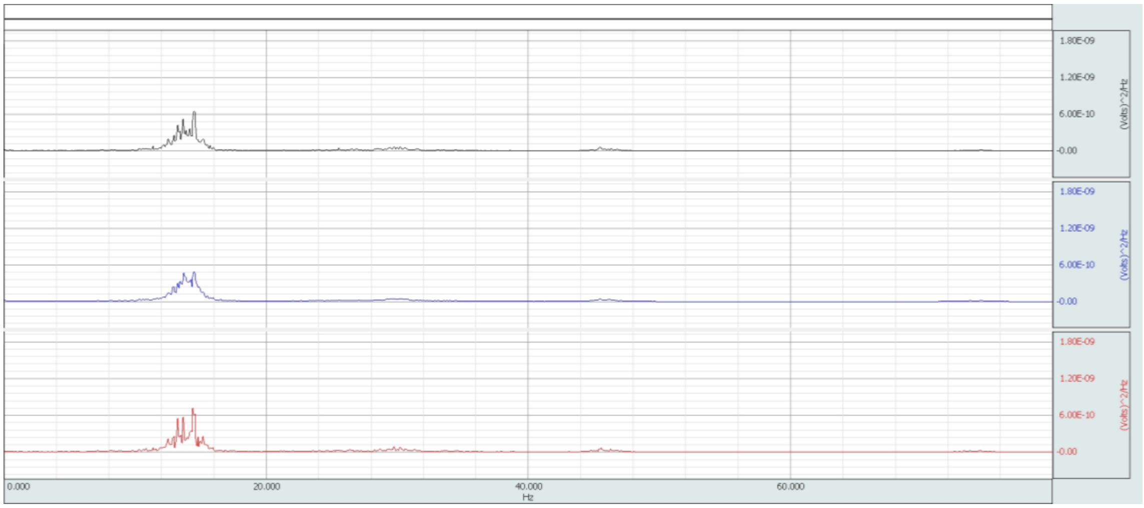

Smooth Artery 3

A. Overlayed View

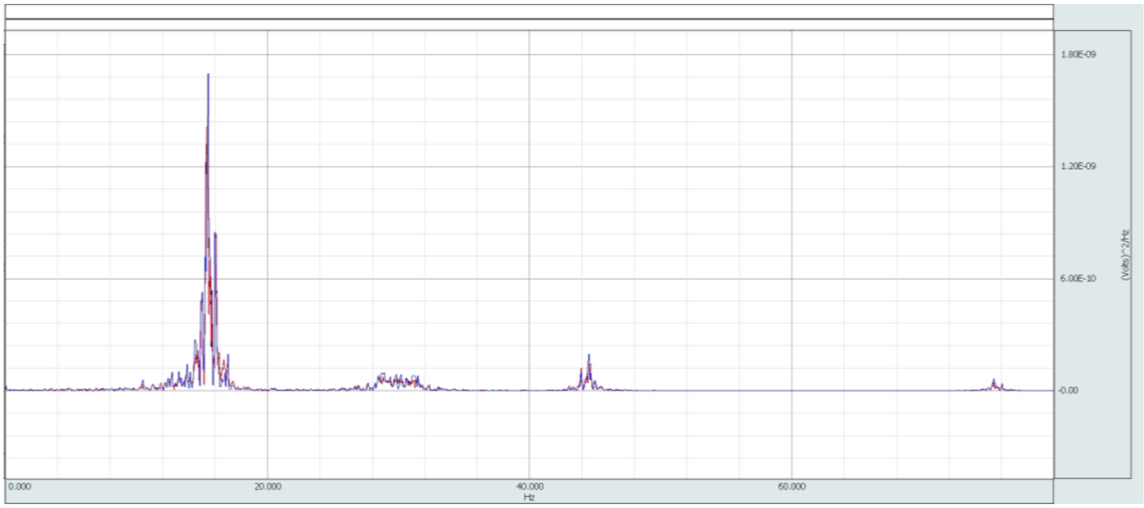

B. Splayed View

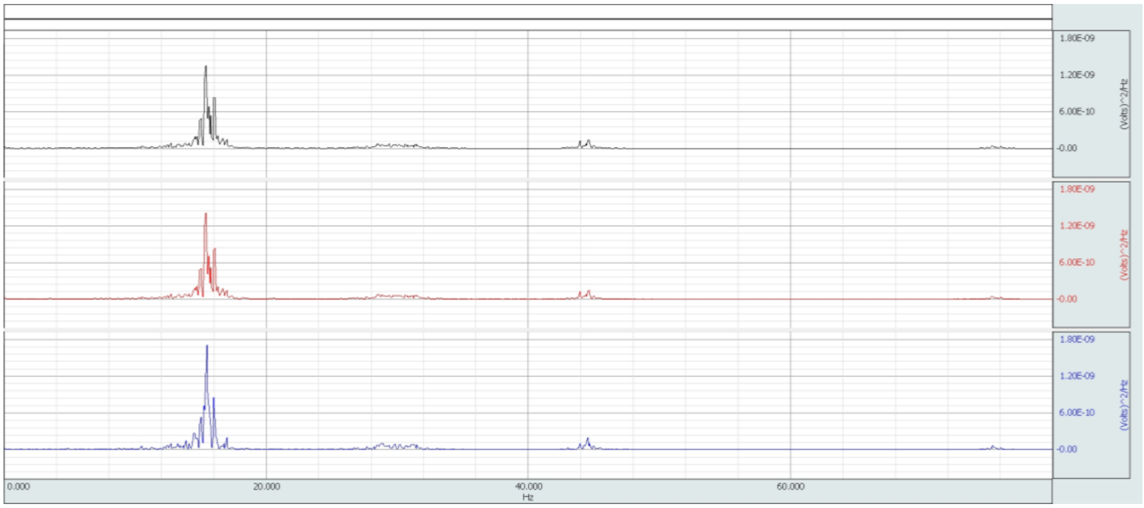

Appendix G. PSD of Rough A Arteries at 0.2 L/min

——— Trial 1

——— Trial 2

——— Trial 3

Rough A Artery 1

A. Overlayed View

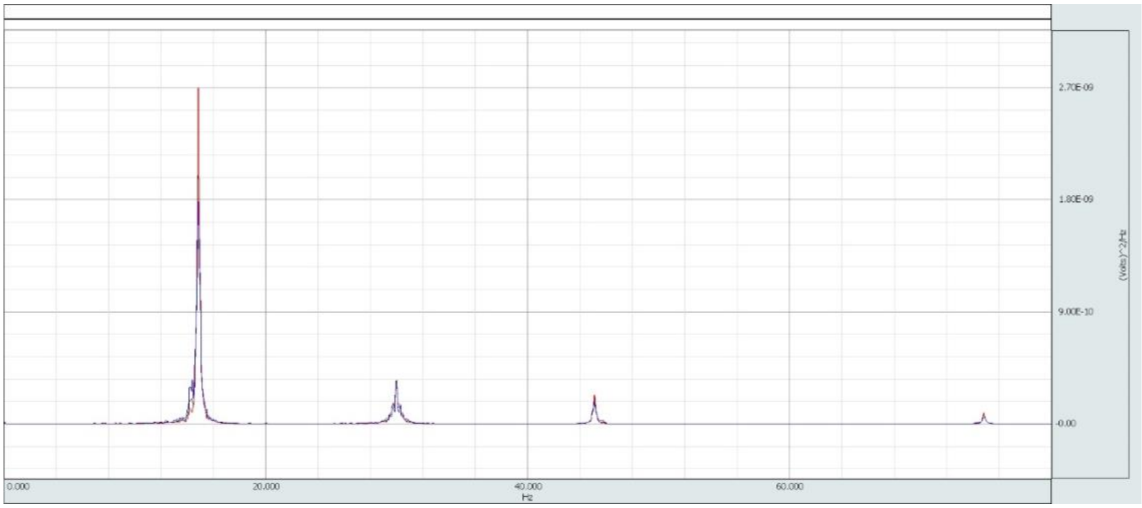

B. Splayed View

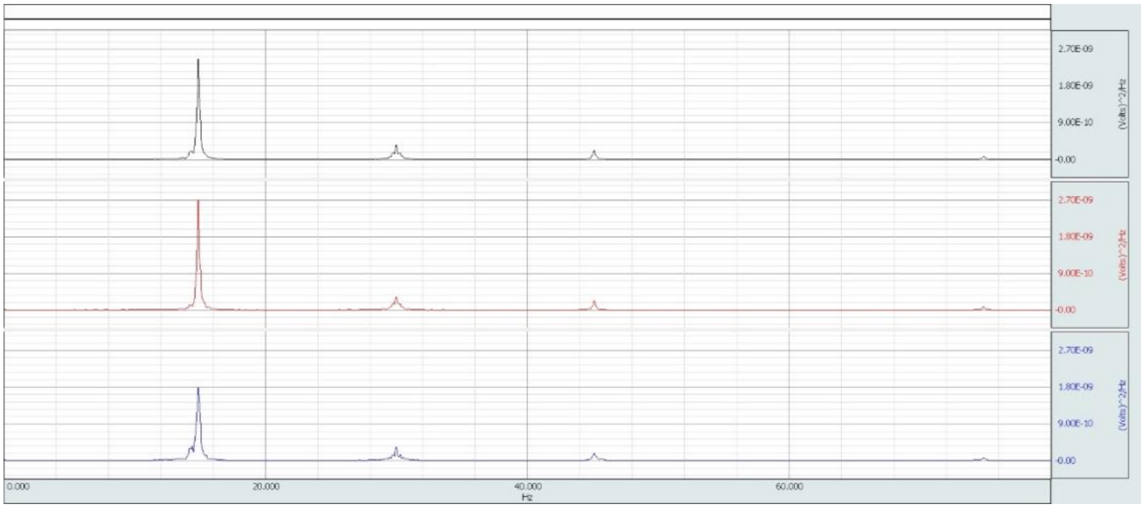

Rough A Artery 2

A. Overlayed View

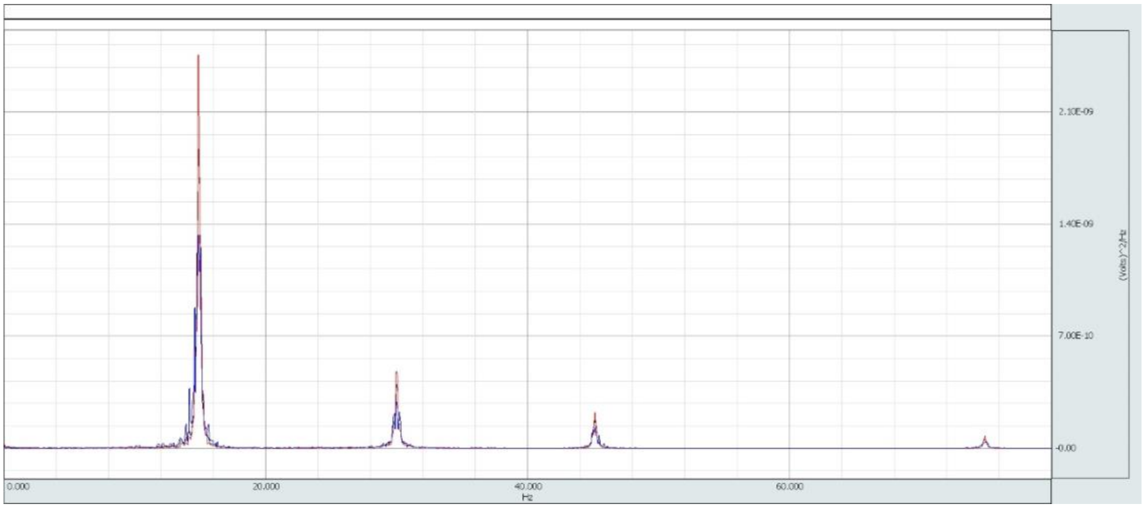

B. Splayed View

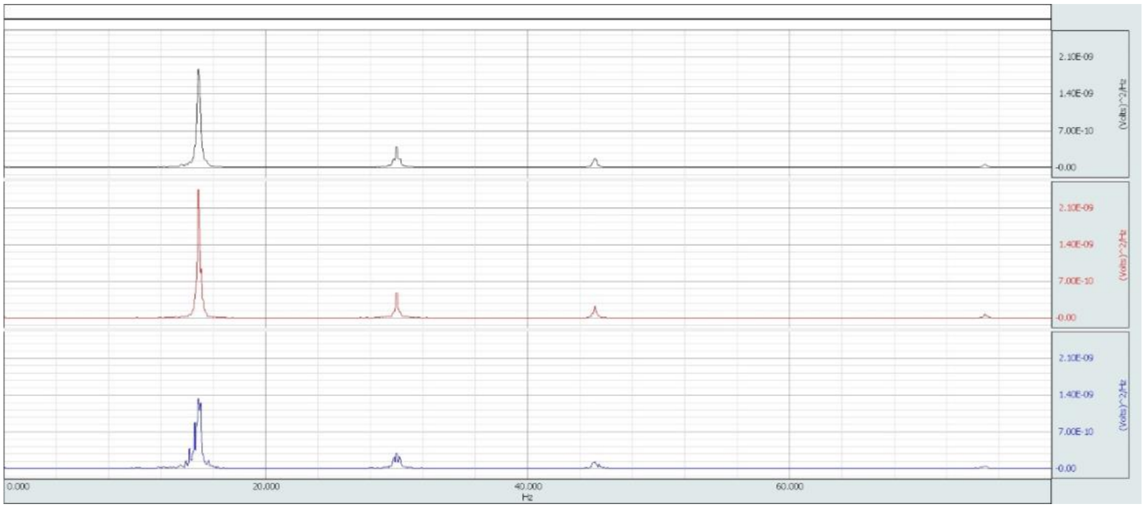

Rough A Artery 3

A. Overlayed View

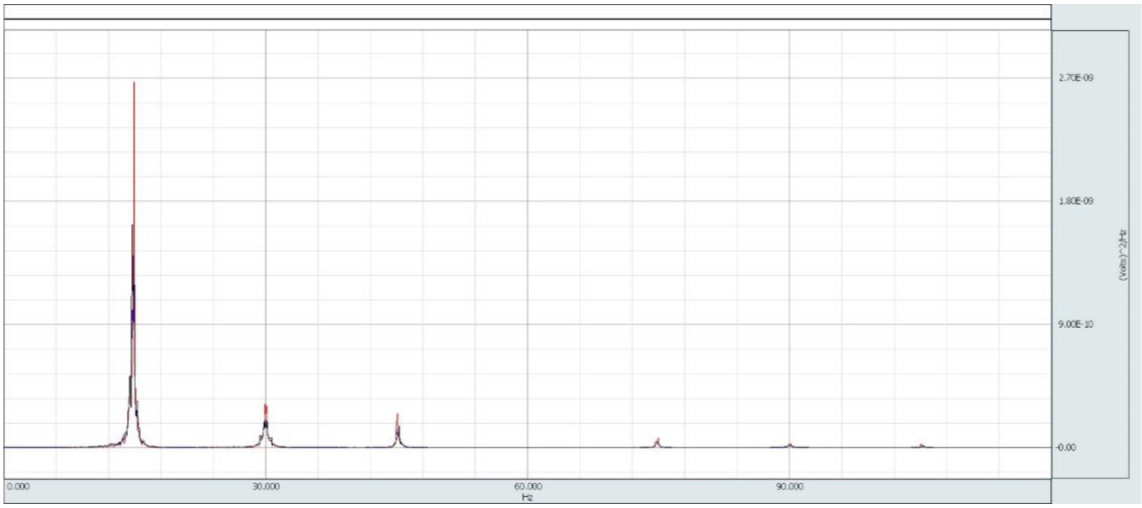

B. Splayed View

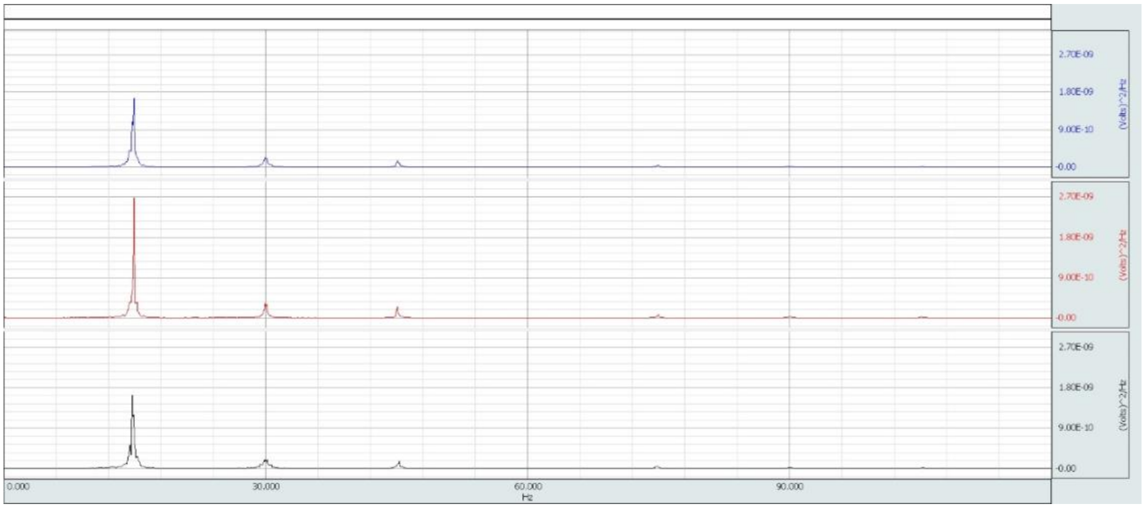

Appendix H. PSD of Rough A Arteries at 1.3 L/min

____ Trial 1

____ Trial 2

____ Trial 3

Rough A Artery 1

A. Overlayed View

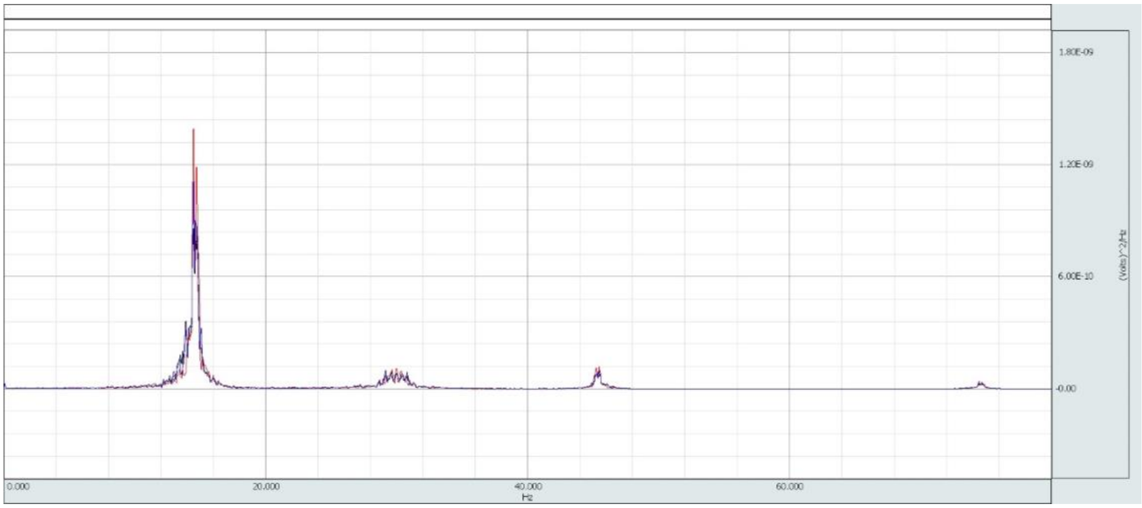

B. Splayed View

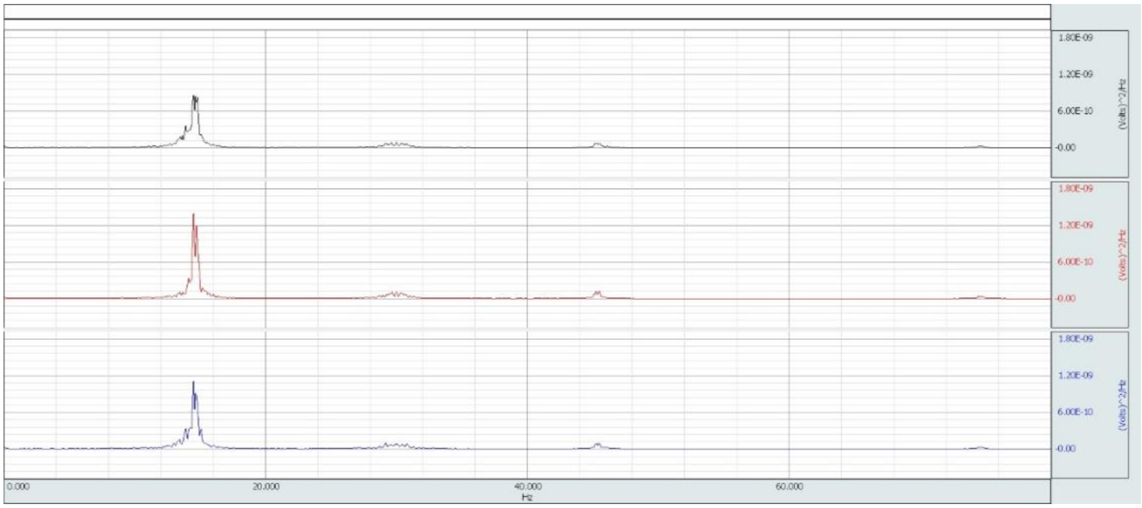

Rough A Artery 2

A. Overlayed View

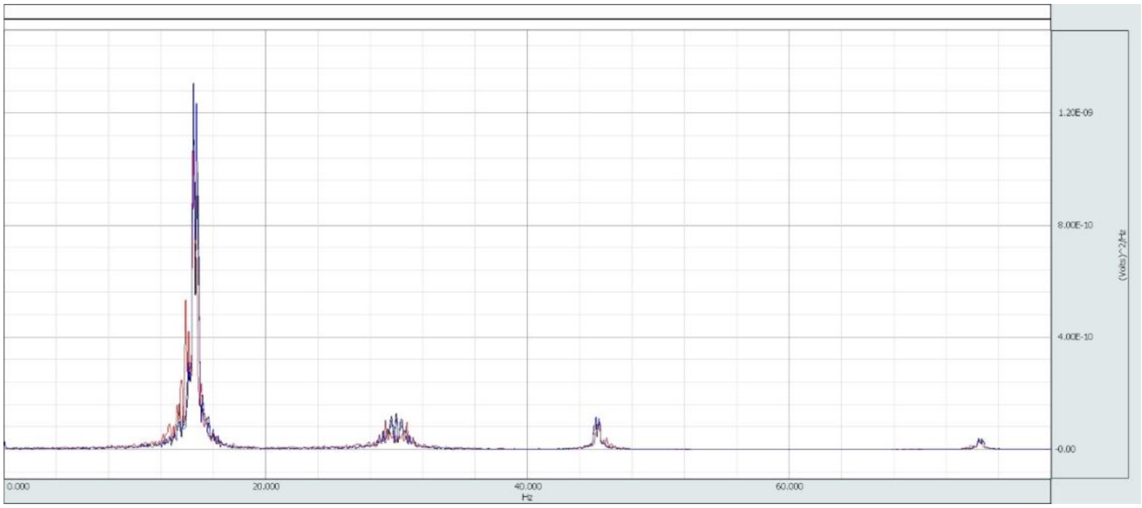

B. Splayed View

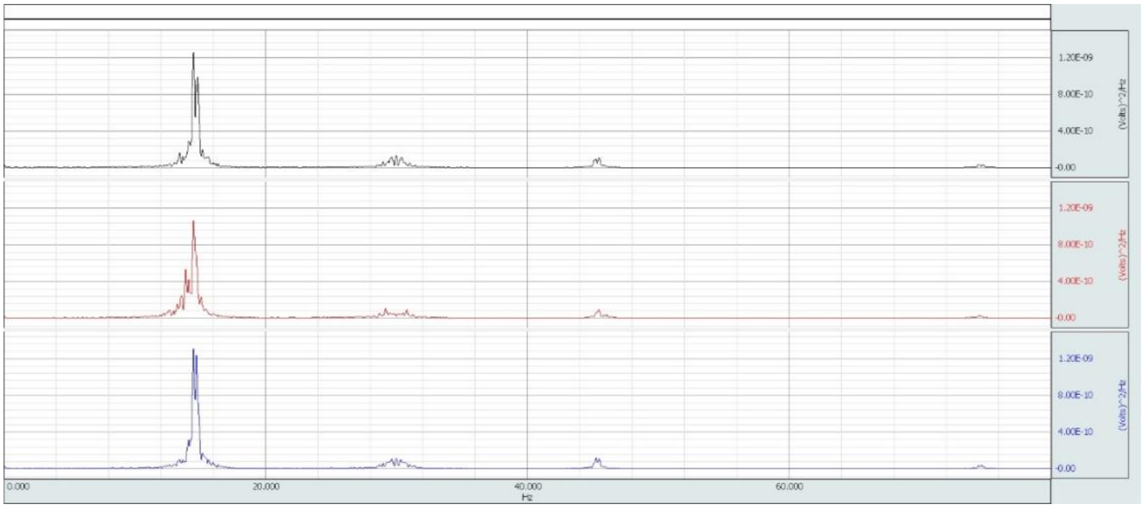

Rough A Artery 3

A. Overlayed View

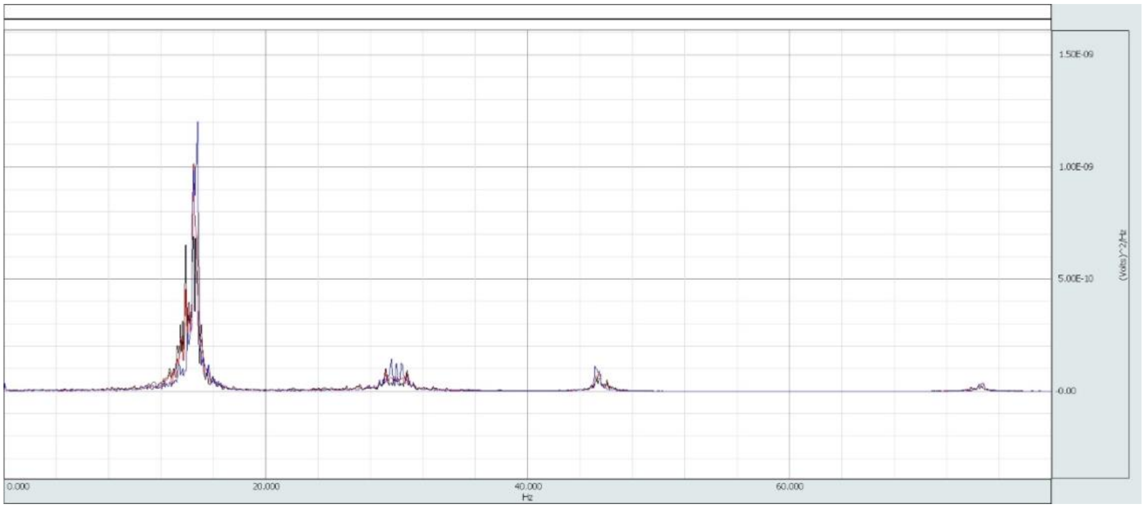

B. Splayed View

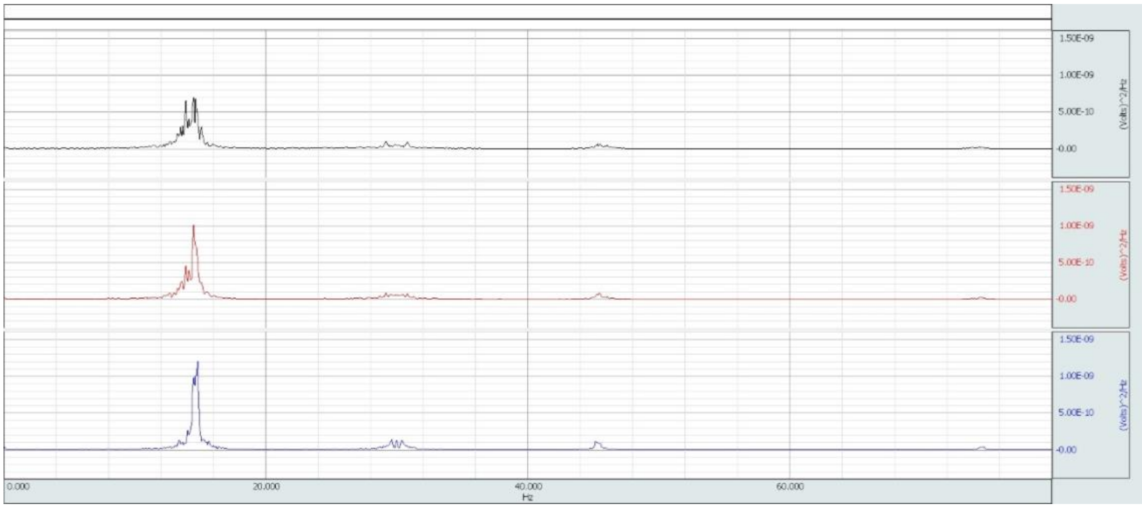

Appendix I. PSD of Rough B Arteries at 0.2 L/min

— Trial 1

— Trial 2

— Trial 3

Rough B Artery 1

A. Overlayed View

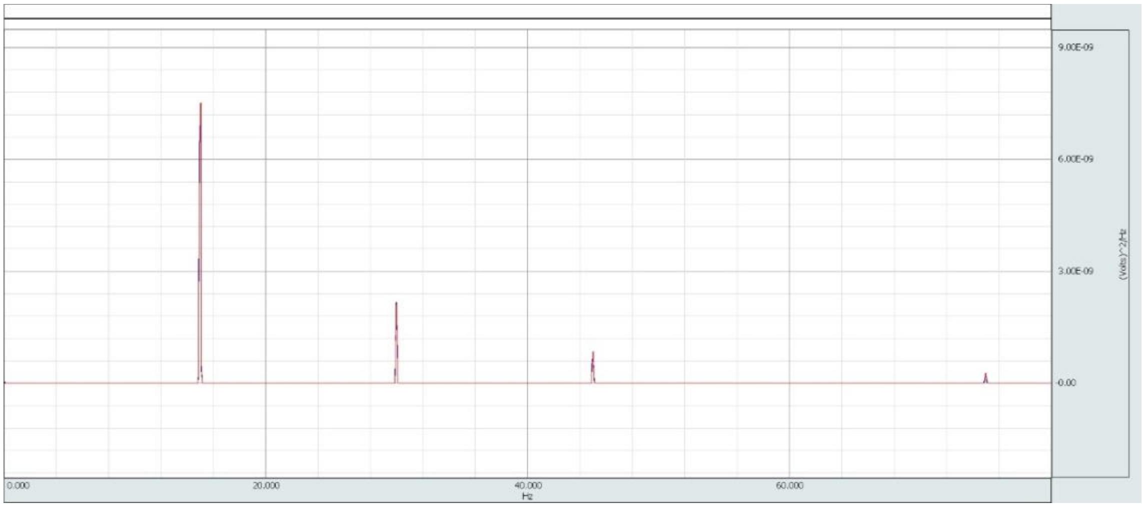

B. Splayed View

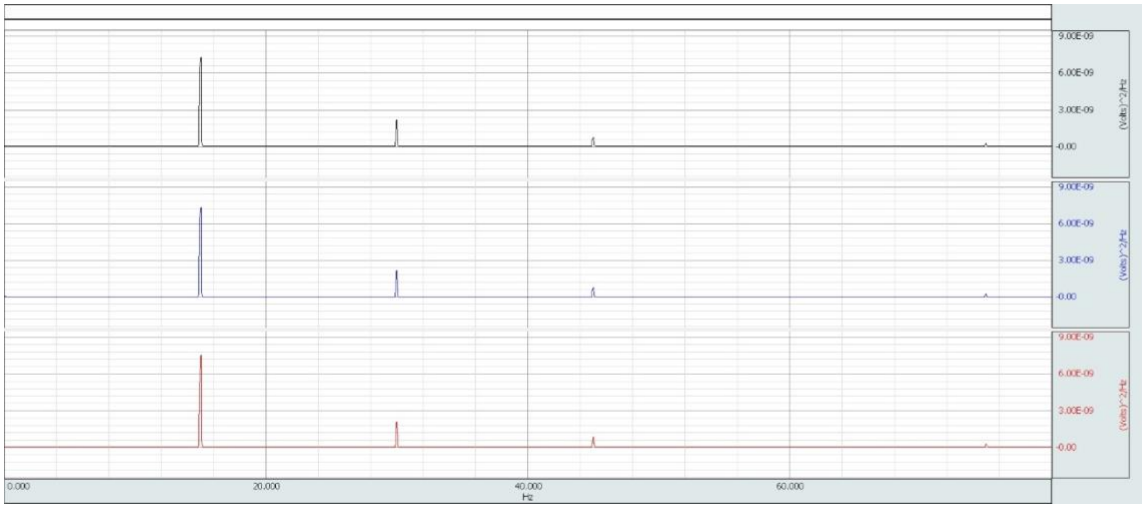

Rough B Artery 2

A. Overlayed View

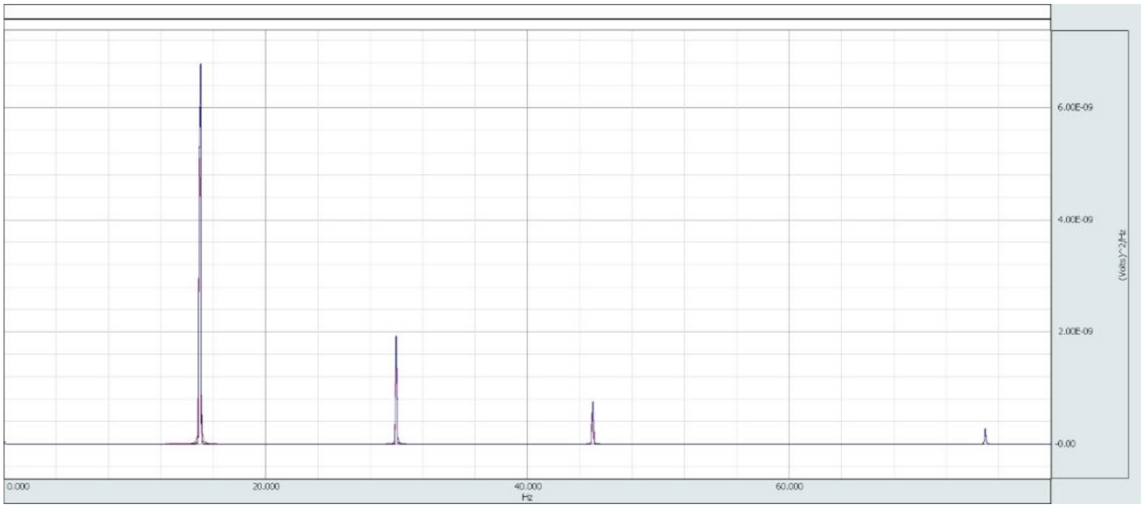

B. Splayed View

Rough B Artery 3

A. Overlayed View

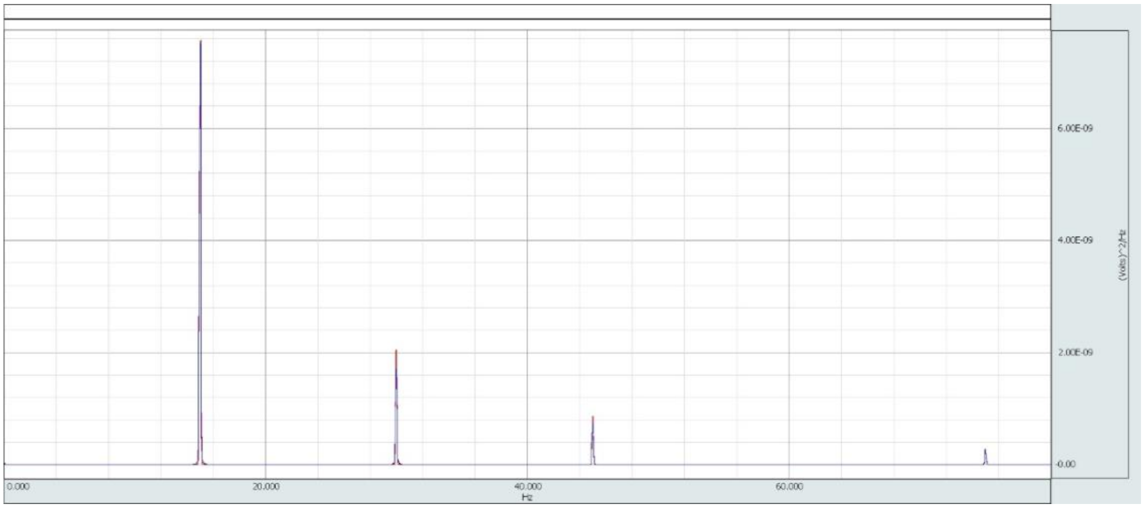

B. Splayed View

Appendix J. PSD of Rough B Arteries at 1.3 L/min

—— Trial 1

—— Trial 2

—— Trial 3

Rough B Artery 1

A. Overlayed View

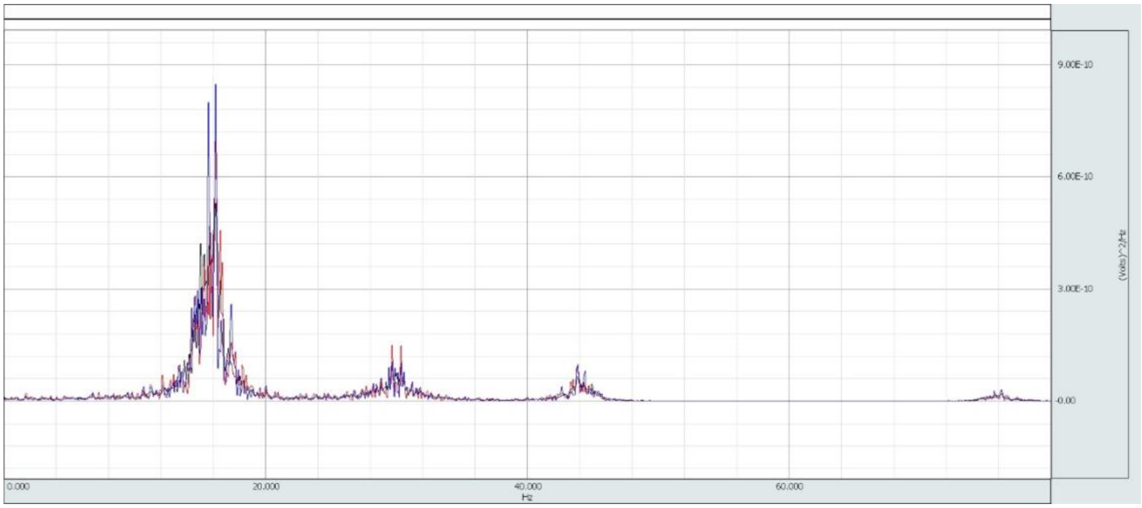

B. Splayed View

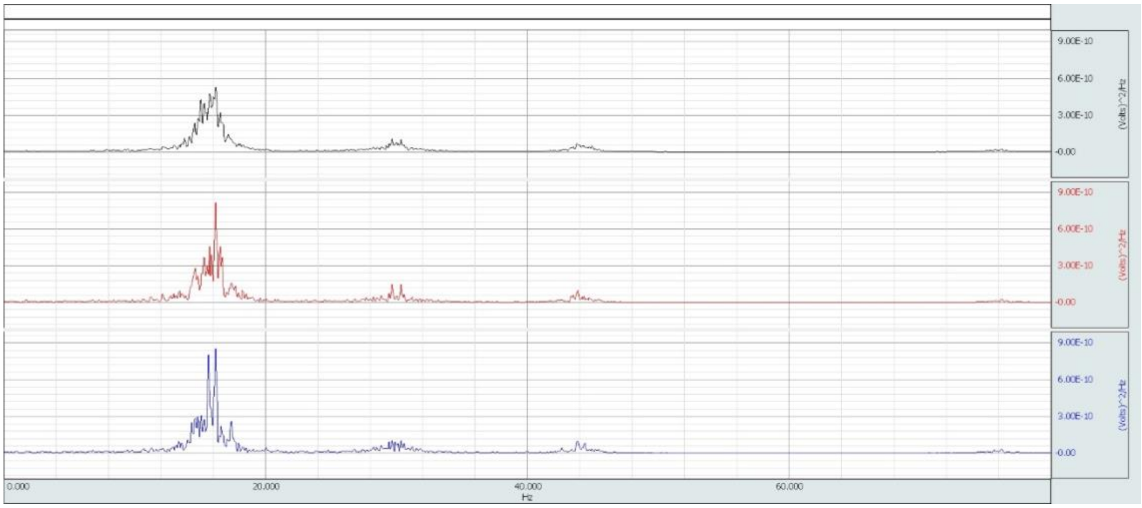

Rough B Artery 2

A. Overlayed View

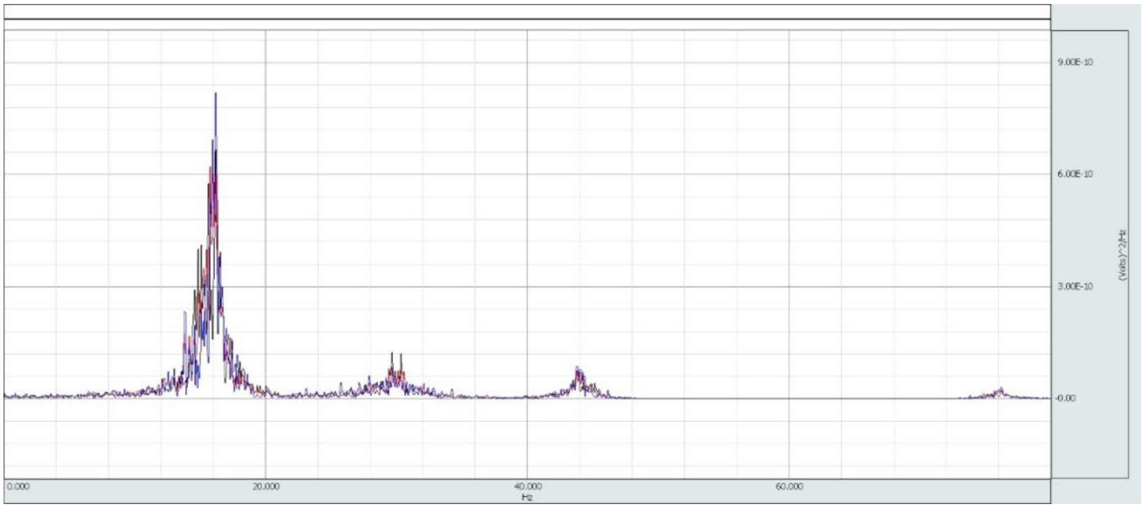

B. Splayed View

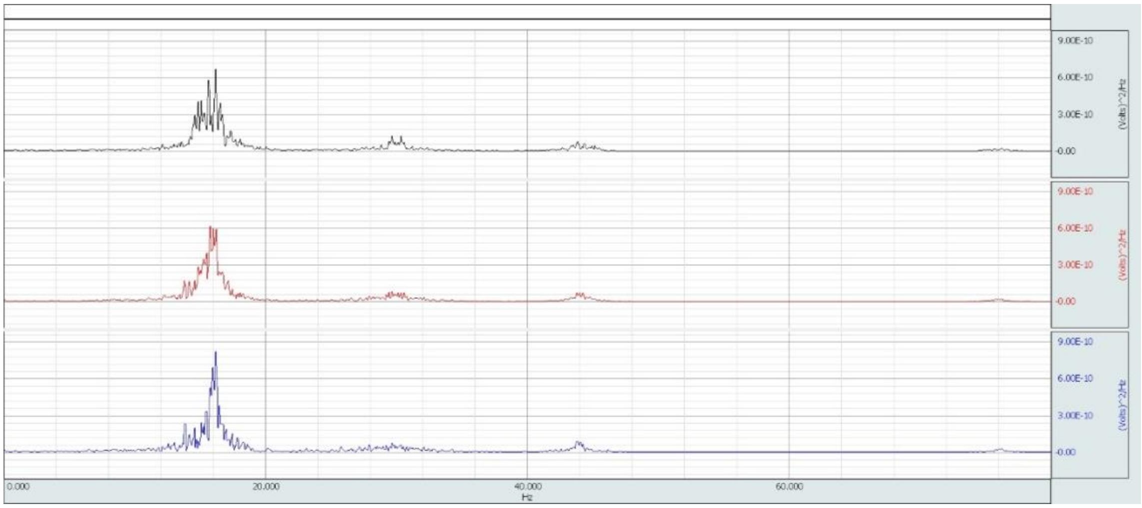

Rough B Artery 3

A. Overlayed View

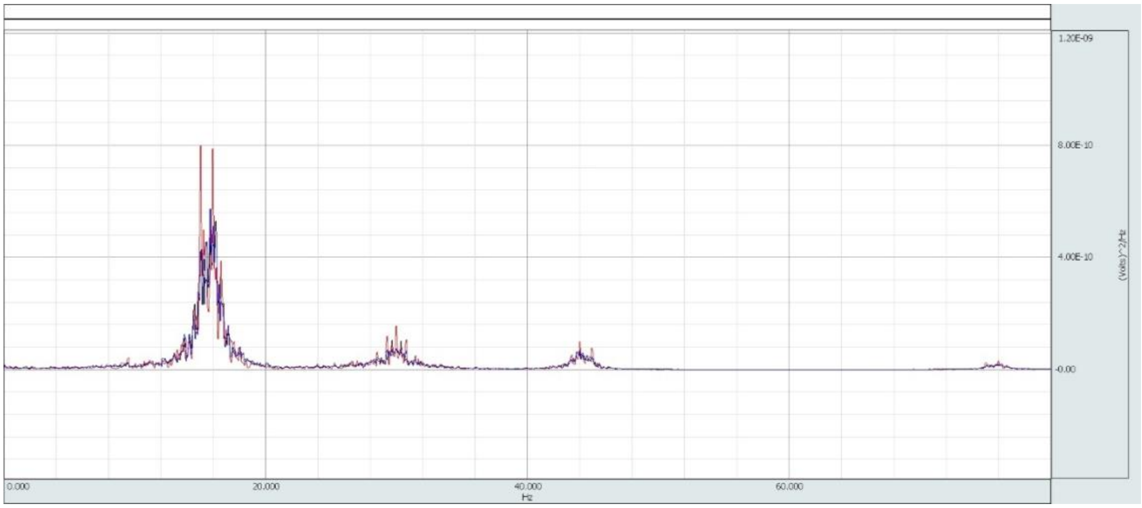

B. Splayed View

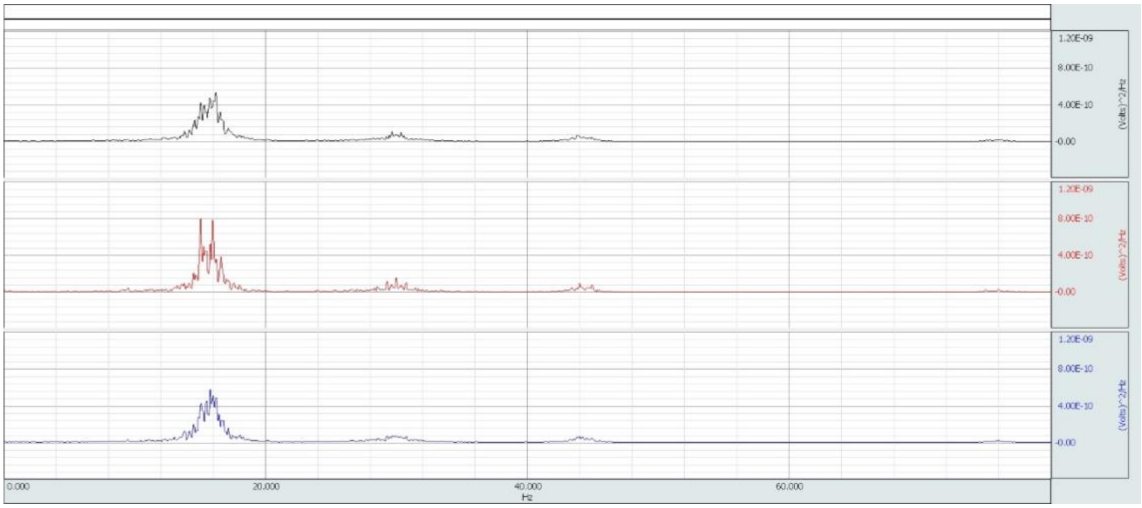

Appendix K. Sample Calculations for Friction Factor Using Bernoulli's Equation

Determining Total Head Losses:

Minor:

1. Contraction

AR = $\frac{A_2}{A_1}$ = $\frac{0.25}{0.375}$ = 0.67

Head loss coefficient, K = 0.198 using Figure ##

$h_{lm} = k*\bar{V}^2/2$

$h_{lm} = 0.0449$

2. Two Tees

Le/D = 20

$h_{lm} = f\left(\frac{L_e}{D}\frac{\bar{V}^2}{2}\right)*2$

$h_{lm} = f(20\bar{V}^2)$

Calculating Friction Factor

$$\left(\frac{p_1}{\rho} + \alpha\frac{\overline{V_1}}{2} + z_1\right) - \left(\frac{p_2}{\rho} + \alpha\frac{\overline{V_2}}{2} + z_2\right) = h_{LT} = h_{lm} + h_L$$

$$\left(\frac{p_1 - p_2}{\rho}\right) = h_{lm} + h_L = 0.0449 + f(20\bar{V}^2) + f\left(\frac{L}{D}\frac{\bar{V}^2}{2}\right)$$

$$\frac{\left(\frac{p_1 - p_2}{\rho}\right) - 0.0449}{20\bar{V}^2 + \frac{L}{D}\frac{\bar{V}^2}{2}} = f$$

For $P_1 - P_2 = 10.385$ (Rough Artery B, Trial 1)

$f = 0.077$

Appendix L. Data Table for Friction Factors for Rough Artery Phantoms

Artery Type		Experimental Friction Factor			
		Trial 1	Trial 2	Trial 3	Average
Rough A	1	0.0699	0.0705	0.0698	0.0701
	2	0.0683	0.0692	0.0727	0.0701
	3	0.0699	0.0682	0.0702	0.0694
Rough B	1	0.0766	0.0786	0.0758	0.0770
	2	0.0774	0.0807	0.0766	0.0782
	3	0.0778	0.0793	0.0759	0.0776

Appendix M. Summary Table of Flow Experiments for All Artery Phantoms

Artery Type		Reynolds Number = 634 Flow Rate = 0.2 L/min				Reynolds Number = 4057 Flow Rate = 1.3 L/min			
		Friction Factor	Average Pressure Drop [mm Hg]	First Frequency Peak [Hz]	Magnitude (V^2/Hz)	Friction Factor	Average Pressure Drop [mm Hg]	First Frequency Peak [Hz]	Magnitude (V^2/Hz)
Smooth	1	0.101	0.1455	11.75	2.44E-09	0.0396	7.781	14.24	6.46E-10
	2	0.101	0.2100	12.05	5.87E-09	0.0396	7.476	14.47	6.15E-10
	3	0.101	0.2390	12.05	3.55E-09	0.0396	7.818	15.45	1.49E-09
Rough A	1	-	0.5410	14.88	2.30E-09	0.0701	9.477	14.50	1.12E-09
	2	-	0.4220	14.88	1.89E-09	0.0701	9.477	14.50	1.21E-09
	3	-	0.6340	14.88	3.55E-09	0.0694	9.392	14.60	9.69E-10
Rough B	1	-	1.6470	15.03	7.37E-09	0.0770	10.384	16.17	7.31E-10
	2	-	1.3590	15.00	5.97E-09	0.0782	10.542	16.20	7.02E-10
	3	-	1.3820	15.03	3.55E-09	0.0776	10.464	16.12	6.34E-10